The Tidal Radius of the Arches Cluster

Matthew W. Hosek Jr.[1], Jessica R. Lu[1], Jay Anderson[2], Andrea M. Ghez[3], Mark R. Morris[3], William I. Clarkson[4]

ABSTRACT

At a projected distance of ∼26 pc from the center of the Milky Way, the Arches Cluster allows us to examine star formation in the extreme environment of the Galactic center (GC). Despite its importance, many key properties such as the size and orbital history of the Arches are not well known. We present an astrometric and photometric study of the outer region of the Arches Cluster (R > 6.25") using the *HST* WFC3IR camera in order to constrain the tidal radius. Using proper motions we separate cluster members from field stars down to F153M = 20 mag (∼2.5 $M_\odot$) over a 120" x 120" field of view, covering an area 144 times larger than previous proper motion studies. This is a significant improvement over photometrically-determined cluster membership (which is affected by the high degree of differential reddening across the field) and allows us to reliably identify cluster members in the outskirts of the cluster. Using the cluster membership probabilities, a derived extinction map, and extensive completeness simulations, we construct the radial profile of the Arches cluster to a radius of ∼80" (∼3.1 pc assuming a distance of 8 kpc). Evidence of mass segregation out to this radius is observed, and no significant tidal tail structures are apparent. We place a 3σ lower limit of 2.9 pc on the tidal radius of the Arches cluster, which is substantially larger than previously assumed (1 - 2.5 pc). We discuss the consequences of this result, which suggests either that the cluster has not come closer than 180 pc to the GC in its lifetime or that it is inflated beyond its nominal tidal radius.

[1]Institute for Astronomy, University of Hawaii, 2680 Woodlawn Drive, Honolulu, HI 96822, USA; mwhosek@ifa.hawaii.edu, jlu@ifa.hawaii.edu

[2]Space Telescope Science Institute, 3700 San Martin Drive, Baltimore, MD 21218, USA; jayander@stsci.edu

[3]UCLA Department of Physics and Astronomy, Los Angeles, CA 90095, USA; ghez@astro.ucla.edu, morris@astro.ucla.edu

[4]Department of Natural Sciences, University of Michigan-Dearborn, 4901 Evergreen Road, Dearborn, MI 48128; wiclarks@umich.edu

1. Introduction

The Arches cluster is a young (2-4 Myr; Najarro et al. 2004, Martins et al. 2008) massive ($\sim 10^4 M_\odot$; Figer et al. 2002; Clarkson et al. 2012) star cluster near the center of the Milky Way. It has a projected distance of just ∼26 pc from the Galactic Center (GC) and is one of the most centrally concentrated star clusters in the Galaxy. Old enough to be free of its natal gas cloud and yet young enough that its stellar population has not been significantly affected by stellar evolution, the Arches cluster provides a unique opportunity to probe how the extreme GC environment affects star formation and cluster evolution. However, studies of the cluster are complicated by stellar crowding and the high level of extinction ($A_V \sim 30$) which varies significantly ($\Delta A_V \sim 15$ mag) across the field (Espinoza et al. 2009; Habibi et al. 2013). This makes it difficult to separate cluster members from field stars through photometric methods. As a result, important questions about the cluster's initial mass function (IMF), structure, and orbit remain.

The IMF of the Arches cluster remains unresolved in the literature. While studies of local stellar populations suggest a universal initial mass function (IMF) above 1 $M_\odot$ (Bastian et al. 2010), conflicting star formation models predict that the dense, high radiation environment near the GC should either favor the formation of high-mass (Morris 1993; Larson 2005) or low-mass (Chabrier et al. 2014) stars. Studies of the present day mass function (PDMF) of the Arches vary significantly, but generally it has been shown to be "top heavy" (favoring high-mass stars) near the center of the cluster and to steepen as a function of radius as a result of mass segregation (Figer et al. 1999; Stolte et al. 2002, 2005; Kim et al. 2006; Stolte et al. 2008; Espinoza et al. 2009; Habibi et al. 2013). However, whether the PDMF is consistent with the "universal" Salpeter IMF ($dN/d\log m \propto m^{-1.35}$; Salpeter 1955) is highly debated. In addition to the effects of mass segregation, these studies are complicated by incomplete observational coverage of the cluster and uncertainties in cluster member identification. A clear determination regarding the consistency of the Arches IMF with the Salpeter IMF would have significant consequences for our understanding of star formation processes.

The orbit of the Arches cluster is only loosely constrained, as well. While its proper motion (Stolte et al. 2008; Clarkson et al. 2012) and doppler velocity (Figer et al. 2002) have been measured, the unknown line-of-sight distance prevents a unique orbital solution. As a result, the birth environment of the cluster, the degree to which it has been modified by the galactic tidal field, and its relation to the nearby Quintuplet cluster are not well understood. For example, it has been suggested that both the Arches and Quintuplet formed at the intersection of the major and minor axes of the central galactic bar, which may be a region of highly efficient star formation (Stolte et al. 2011, 2014). Alternatively, the Arches may be the end product of a starburst cluster formation sequence identified by Longmore et al. (2013) and Kruijssen et al. (2014), where starburst clusters are formed from tidally-compressed gas clouds that pass close to the GC. It has also been suggested that the Arches may be a possible source of the isolated massive stars observed near the GC (Mauerhan et al. 2010; Habibi et al. 2014). Clearly, understanding the orbit of the cluster is necessary in order to place it in proper context within the galactic environment.

In a first step to address these major questions, we reliably identify cluster members out to large radii (∼90") via astrometry, measuring the large scale structure of the cluster and constraining its tidal radius for the first time. By using proper motions rather than photometry for cluster membership, many of the difficulties caused by differential reddening are avoided. The effectiveness of this method on the Arches cluster was demonstrated by Stolte et al. (2008) and Clarkson et al. (2012), who use ground-based adaptive optics (AO) observations to measure the cluster's bulk proper motion and identify members in the central 10" x 10" region. We expand upon these studies using *Hubble Space Telescope* (HST) observations, which provide high astrometric precision over a field of view 144 times larger (120" x 120"). This allows us to measure the stellar radial density profile out to the predicted tidal radius (25" - 60"; Kim et al. 2000; Portegies Zwart et al. 2002; Habibi et al. 2013), examine mass segregation to the outskirts of the cluster, and search for the presence of tidal tails. In addition, the constraint on the tidal radius provides insight to the cluster's orbit. Since the age of the Arches is significantly less than its relaxation time ($t_{rh} \sim 10^7$ yrs), its tidal radius is set by the closest approach to the GC, where it experiences the strongest tidal field. If the distance of closest approach is known, then the range of possible orbits for the cluster calculated by Stolte et al. (2008) can be significantly delimited. Based on our constraint on the tidal radius, we present a rough calculation of the minimum GC approach of the Arches cluster and discuss the consequences of this result. An accurate determination of the PDMF of the Arches cluster as well as full numerical modeling of its orbit are left to future papers.

2. Methods

2.1. Observations and Measurements

We observed the Arches cluster with the *Hubble Space Telescope* (HST) WFC3IR camera using the F127M, F139M, and F153M filters (1.27 μm, 1.39 μm, and 1.53 μm, respectively; PI: Ghez, ID: 11671, 12318, 12667). A description of these observations is provided in Table 1. These observations are centered at coordinates α(J2000) = 266.4604, δ(J2000) = -28.8222 and have a field of view of 120" x 120" (Figure 1). Astrometry is performed on the F153M observations, which were obtained in three epochs over a two year baseline: 2010.604, 2011.683, and 2012.616. Of this filter set, F153M is best for astrometry because it is the longest-wavelength medium-band filter and provides the optimal combination of limited saturation and a well-sampled point spread function (PSF) with a FWHM ∼0.17" (1.4 pixels, scale = 0.121" pix^{-1}). By observing at the same position angle and pixel position across epochs and using a sub-pixel spiral dithering pattern within each epoch, we are able to achieve high astrometric and photometric precision. F127M and F139M observations were only obtained in 2010.634 using a simpler dither pattern for the purpose of color information to derive extinction.

We use a combination of public and custom software to extract high-precision astrometry and photometry from the observations, described in detail in [APPENDIX 1]. The final measurements

for each filter/epoch are obtained from PSF-fitting using a spatially-variable PSF model. Star positions are transformed to a common astrometric reference frame (arbitrarily chosen to be 2010 F153M) using general 6-parameter linear transformations that can be described as a 2D translation, rotation, plate scale, and shear for each image. Approximately ∼50,000 stars are measured in each filter/epoch, reaching F127M = 23.63 mag, F139M = 23.29 mag, and F153M = 23.31 mag. The photometry is calibrated to the standard Vega magnitude system using the zero points derived for the WFC3IR camera[1]. An analysis of the astrometric and photometric errors is provided in [APPENDIX 1] as well.

Proper motions are derived for stars that are detected in all three F153M epochs, and we restrict the forthcoming analysis to this sample. Proper motion uncertainty as a function of observed F153M magnitude is presented in Figure 2. Several tests were conducted to confirm the validity of these errors (see [APPENDIX 1]). Previous studies of the bulk proper motion of the Arches cluster relative to the field population by Stolte et al. (2008) and Clarkson et al. (2012) revealed that a precision of ∼0.8 mas yr^{-1} is needed in order to reliably separate cluster members from field stars. As a conservative error cut we require a minimum proper motion precision of 0.65 mas yr^{-1}, which we achieve down to F153M ≈ 20 mag. At the average distance and reddening of the Arches cluster this corresponds to roughly 2.5 M$_\odot$. We additionally require a minimum photometric precision of 0.06 mags in each F153M epoch to ensure high-quality results. Of the ∼50,000 stars measured in each filter/epoch we obtain ∼26,000 proper motions, ∼4500 of which pass these error cuts. Slightly more stars are trimmed by the photometric cut than the astrometric cut. The kinematic distinction between cluster and field stars is clear in a vector point diagram (VPD; v_x vs. v_y) of this high-quality proper motion sample (Figure 3).

2.2. Cluster and Field Populations

In order to identify individual Arches members via proper motion we must first determine the kinematic distributions of the cluster and field populations. Previous studies have assumed that these populations can be modeled as a circular and elliptical bivariate Gaussian distribution in a VPD, respectively (Clarkson et al. 2012). The ellipticity of the field distribution is observed because it is primarily composed of stars in the galactic bulge that exhibit a larger velocity dispersion parallel to the galactic plane than perpendicular to it, a consequence of coherent rotation (Clarkson et al. 2008; Howard et al. 2009; Kunder et al. 2012). While the field population isn't strictly Gaussian, it is a first approximation that is commonly used in studies of open clusters (e.g. Sanders 1971; Jones & Walker 1988; Kozhurina-Platais et al. 1995). As discussed in § 3.2, the number of field contaminants within the cluster sample matches what would be predicted given the fitted distributions, indicating that this assumption is adequate for our purposes. A more complete description of the field requires modeling the stellar density, kinematics, and reddening at all distances along our line of sight

[1]As of August 2014; http://www.stsci.edu/hst/wfc3/phot_zp_lbn

towards the Arches. Such an analysis may be useful for exploring Galactic structure but is beyond the scope of this paper.

Following Clarkson et al. (2012), we construct a likelihood function for each star from a sum of the two bivariate gaussian components:

$$L(\boldsymbol{v}_i) = \sum_{k=0}^{1} \pi_k \frac{1}{2\pi|\boldsymbol{\Sigma}_{ki}|} exp\left(-\frac{1}{2}(\boldsymbol{v}_i - \boldsymbol{\mu}_k)^T \boldsymbol{\Sigma}_{ki}^{-1}(\boldsymbol{v}_i - \boldsymbol{\mu}_k)\right) \tag{1}$$

where k = 0, 1 represents the circular cluster and elliptical field gaussian distributions, $\boldsymbol{v}_i$ is the proper motion of the ith star, π_k is the fraction of total stars in the kth gaussian such that $\sum_{k=0}^{1} \pi_k = 1$, $\boldsymbol{\mu}_k$ is the velocity centroid of the kth gaussian, and $\boldsymbol{\Sigma}_{ki}$ is the covariance of kth gaussian and ith star. Since the population model and stellar proper motion errors are both Gaussian their covariance matrices add such that $\boldsymbol{\Sigma}_{ki} = \boldsymbol{S}_i + \boldsymbol{Z}_k$, where $\boldsymbol{S}_i$ is the velocity error matrix (assumed to be diagonal with velocity error components $\sigma_{v_x}^2$ and $\sigma_{v_y}^2$) and $\boldsymbol{Z}_k$ is the covariance matrix of the kth gaussian fit.

With the likelihood function defined, we can determine the global kinematic parameters of the cluster and field populations through Bayesian inference using Bayes' theorem:

$$P(\boldsymbol{\mu}, \boldsymbol{Z}|\pi_c, \boldsymbol{v}, \boldsymbol{S}) = \frac{P(\pi_c, \boldsymbol{v}, \boldsymbol{S}|\boldsymbol{\mu}, \boldsymbol{Z})P(\boldsymbol{\mu}, \boldsymbol{Z})}{P(\pi_c, \boldsymbol{v}, \boldsymbol{S})} \tag{2}$$

where $P(\boldsymbol{\mu}, \boldsymbol{Z}|\pi_c, \boldsymbol{v}, \boldsymbol{S})$ is the posterior probability of our model parameters $(\boldsymbol{\mu}, \boldsymbol{Z})$, the velocity centroid and covariance matrix of our gaussian models, given the fraction of cluster members π_c, observed velocity distribution $\boldsymbol{v}$, and velocity error matrix $\boldsymbol{S}$; $P(\pi_c, \boldsymbol{v}, \boldsymbol{S}|\boldsymbol{\mu}, \boldsymbol{Z})$ is the probability of the observed stellar velocity distribution given the model; and $P(\boldsymbol{\mu}, \boldsymbol{Z})$ is the prior probability of the model. In this case $P(\pi_c, \boldsymbol{v}, \boldsymbol{S}|\boldsymbol{\mu}, \boldsymbol{Z}) = \sum_i^N \log L(\boldsymbol{v}_i)$, where N is the total number of stars in the sample. A summary of the model parameters is provided in Table 2.

For the purposes of the kinematic fitting, we transform the proper motions into the reference frame of the cluster by subtracting the bulk motion of the cluster from all stellar velocities. We determine the bulk proper motion of the cluster from the mean motion of stars in the central 10" x 10" of the cluster, since cluster members dominate this region. We use the results of Clarkson et al. (2012) to inform the priors for the cluster and field kinematic dispersions as well as the orientation of the field kinematic ellipse with respect to our observations, and adopt a broad uniform prior for all other parameters.

To find the maximum posterior probability for each parameter we use *Multinest*, a publicly available nested sampling algorithm which serves as an alternative to Markov Chain Monte Carlo (MCMC) algorithms when exploring multi-modal parameter spaces (Feroz et al. 2009, 2013). This iterative technique calculates the Bayesian evidence, $P(\boldsymbol{\mu}, \boldsymbol{Z}|\pi_c, \boldsymbol{v}, \boldsymbol{S})$, at a fixed number of points

in the parameter space and identifies possible peaks, restricting subsequent sampling to the regions around these peaks until the change in evidence drops below a user-defined tolerance level. Multiple peaks can be identified and evaluated, resulting in increased sampling efficiency with complicated parameter spaces. We find that using 1000 sample points and a tolerance of 0.3 is sufficient to determine the best parameters for our model.

The one-dimensional posterior distributions for the free parameters in our cluster and field population model are shown in Figure 4. We fit a Gaussian distribution to each posterior to determine the best-fit parameter values and their errors, which are presented in Table 2. The fitted kinematic distribution of the cluster and field populations is overlaid on the VPD in Figure 5. The long axis of the field distribution has a position angle of -12.5° relative to our observations (PA = -45°), consistent with the Galactic plane. In principle, we could derive the bulk proper motion of the Arches cluster with respect to the GC from the difference in the kinematic centers of the cluster and field populations as is done by Stolte et al. (2008) and Clarkson et al. (2012). However, it is uncertain if the observed field bulge population is kinematically centered on the GC due to a bias toward observing stars on the near side of the bulge. A careful determination of the Arches proper motion in the reference frame of the GC is left to a future paper.

2.3. Extinction Map Using Red Clump Stars

Taking advantage of the high photometric precision of the HST observations, we use red clump (RC) stars to measure the extinction across the Arches cluster field. This provides an alternative to "sliding" apparent cluster members along their reddening vector in a color-magnitude diagram (CMD) to a theoretical cluster isochrone to determine extinction, as has been done in previous studies of the Arches cluster (Kim et al. 2006; Espinoza et al. 2009; Habibi et al. 2013). This CMD sliding method is prone to field contamination and isochrone uncertainties, especially at the pre-main sequence turn-on point at low to moderate masses. On the other hand, stellar evolution theory and observations show that RC stars exhibit well-defined luminosities and colors which do not vary significantly with age or metallicity (Castellani et al. 1992; Paczynski & Stanek 1998; Stanek et al. 2000), making them useful calibrators to measure extinction. This is especially true near the galactic center, where large numbers of RC stars among the bulge population have made it possible to create reddening maps of different regions (Sumi 2004; Schödel et al. 2010). Though the line-of-sight position of the Arches with respect to the bulge RC stars is uncertain, we assume the majority of the extinction is caused by foreground dust and that the RC population exhibits similar reddening as the cluster members themselves. Using this approach we create the first RC-based extinction map of the Arches cluster (Figure 6).

RC stars are identified and their extinction determined from the F127M vs. [F127M - F153M] (roughly J vs. [J - H]) CMD as described in [APPENDIX 2]. The IR reddening law derived for the GC by Nishiyama et al. (2009) is used to calculate A_λ at different wavelengths. We spatially interpolate these extinction values across the field using a 5th order bivariate spline to determine

the extinction at each image pixel. The median error on this extinction map is ∼0.1 mag in A_{Ks}, calculated from the error on the mean of RC star extinction residuals in 15" bins. Extinction values range from $1.8 < A_{Ks} < 3.0$ with an median of $A_{Ks} = 2.4$ for cluster members. This range is in agreement with the reddening map of Habibi et al. (2013), who find $1.6 < A_{Ks} < 3.3$ also using a Nishiyama et al. (2009) reddening law.

2.4. Completeness Analysis

In order to accurately measure the radial density profile of the Arches Cluster we conduct an extensive completeness analysis on our astrometry pipeline. In addition to the sensitivity threshold of our observations, stars may be missed due to source confusion and proximity to bright and/or saturated stars. These effects are especially relevant for the dense central region of the cluster. To quantify our completeness we conduct an artificial star injection and recovery test, randomly planting 400,000 stars in each image and determine which are recovered to sufficient accuracy and precision as a function of spatial position and magnitude. The magnitudes of the artificial stars are drawn from the observed CMD of the field in order to best simulate the photometric properties of the observed stars. These magnitudes are then perturbed by a random amount drawn from the Gaussian photometric uncertainty of the real star they are simulating in order to encapsulate the photometric errors. The same set of artificial stars is applied to all observations. This analysis assumes that the artificial star measurement errors match those of the observed stars, which we test and discuss in [APPENDIX 3].

The conditions under which an artificial star is considered as recovered matches the error cuts and criteria applied to the real data. Within a given epoch, a recovered artificial star must: 1) be detected in at least 75% of the images within that epoch; 2) have position and magnitude errors less than 1.5 mas (required for a proper motion precision better than or equal to 0.65 mas yr^{-1}) and 0.06 mag, respectively; and 3) have a measured position and magnitude within 0.5 pix (60 mas) and 0.5 mag of the planted values to guard against misidentification. An additional requirement that the artificial star be recovered in all 3 F153M epochs is applied as this is required of observed stars in order to calculate their proper motions (§ 2.1). The fraction of recovered artificial stars to the total number of artificial stars represents the completeness fraction. Using the RC-derived extinction map, artificial star magnitudes are corrected to the mean reddening of the field ($A_{Ks} = 2.4$) to allow for consistent analysis across the wide range of extinction. The resulting completeness curves as a function of magnitude and of radius are presented in Figure 7. We achieve greater than 50% completeness down to F153M = 20 averaged across the full field. However, the completeness in the inner 6.25" (∼0.25 pc at 8 kpc[2]) of the cluster is significantly lower due to stellar crowding, falling to 30% by F153M = 18.5. As a result, we restrict the following analysis to stars with R > 6.25" and a differentially de-reddened magnitude brighter than F153M = 20.

[2]All distances throughout assume a distance of 8 kpc to the Arches cluster.

3. Results

3.1. Cluster Membership

With the kinematic properties of the cluster and field populations determined (§ 2.2), we calculate the probability of cluster membership for each star based on its proper motion:

$$P_{member} = \frac{P_{cluster}}{P_{cluster} + P_{field}} \tag{3}$$

where $P_{cluster}$ and P_{field} are the probabilities calculated using the gaussian components in Equation 1. A histogram of the resulting cluster membership probabilities is shown in Figure 8. We identify stars with $P_{member} \geq 0.85$ as cluster members, yielding 523 out of the ∼4500 stars that survived the described error cuts. The distribution of these stars in both position and velocity space is shown in Figure 9. We note that the results presented in this study are not significantly affected by adjusting this membership threshold.

By applying the extinction map derived in § 2.3 to the identified cluster members we create a differentially de-reddened F127M vs (F127M - F153M) CMD of the cluster (Figure 10). The improvement between this CMD and the uncorrected CMD is dramatic in both the color dispersion and the definition of the blue edge. The scatter along the redward edge of the cluster may be caused by intrinsic reddening of the objects themselves, which is not unexpected given the young age of the Arches. The presence of circumstellar disks in the cluster has been confirmed by previous photometric studies (Stolte et al. 2010). The objects to the blue of the blue edge are likely foreground sources that happen to have a proper motion similar to that of the cluster.

The mean extinction of all cluster members is $A_{Ks} = 2.42 \pm 0.14$ mag, calculated using a Nishiyama et al. (2009) extinction law. The inner region of the cluster (R < 10", or R < 0.4 pc) exhibits a tight range of reddening values from $2.33 < A_{Ks} < 2.53$, while the outer region of the cluster (R > 10") exhibits a much wider range from $2.04 < A_{Ks} < 2.76$. The larger dispersion in the outer region can be attributed to significant differential reddening across the field. These values are consistent with the literature, although there are variations due to different methodologies and reddening laws. Habibi et al. (2013) find $A_{Ks} = 2.6 \pm 0.2$ mag for 0.2 pc < R < 0.4 pc and $A_{Ks} = 2.6 \pm 0.3$ mag for 0.4 pc< R < 1.5 pc using the CMD sliding method and the Nishiyama et al. (2009) extinction law. Also using the CMD sliding method, Espinoza et al. (2009) and Kim et al. (2006) find higher values of $A_{Ks} = 2.97$ and 3.1 for R < 0.4 pc using the extinction laws of Fitzpatrick (2004) and Rieke et al. (1989), respectively.

3.2. Radial Density Profile

We construct the radial profile of the Arches Cluster using the Bayesian analysis method described by Do et al. (2013). This allows us to construct an un-binned profile that simultaneously incorporates the image completeness, cluster membership probability, and an area correction to account for incomplete field coverage at large radii due to the finite field of view. To ensure that the profile reaches a uniform depth across the image and a reasonable completeness correction can be made, only stars with differentially de-reddened ($A_{Ks} = 2.4$) magnitudes of F153M ≤ 20 are considered. We also do not attempt to calculate the profile at cluster radii less than 6.25" (0.25 pc) due to incompleteness (§ 2.4). We adopt a single power law as our likelihood function and calculate the posterior distribution for the slope Γ and the field contamination b:

$$L_i(r, \Gamma, b) = A * r^{-\Gamma} + b \tag{4}$$

$$P(D|\Gamma, b) = \sum_{i}^{N} \log L_i(r, \Gamma, b) * (P_i/(I_i * A_i))$$

where $P(D|\Gamma, b)$ is the probability of observing the data (D) given the model, P_i is the membership probability of the ith of N total stars, I_i is the completeness at that star's radius, and A_i is the relative fraction of observed area at the star's radius relative to an infinite field of view ($A_i < 1$ for radii greater than 60", or 2 pc). The field contamination b is assumed to be a constant across the image. An uninformed prior is used for b and Γ, and the amplitude A is calculated such that the integral of the radial profile over the image yields the total number of cluster members observed after membership probability, completeness, and area corrections. A summary of our best-fit model and subsequent results are presented in Table 3 and Figure 11. A binned radial profile is included for comparison. The posterior distributions for these parameters are presented in [APPENDIX 4].

To quantitatively assess whether the power-law model is an appropriate one for the observed profile we conduct a posterior predictive analysis using χ^2 as the test statistic (Gelman et al. 2013). We randomly select 1000 sets of model parameters from the joint posterior distribution and generate artificial binned profiles from these models. Each data point within the artificial profiles is shifted by an offset randomly drawn from a normal distribution of width equal to the uncertainty in that value, calculated by combining the poisson uncertainty from the number of stars in the bin and the uncertainty in the completeness correction in quadrature. We then calculate a χ^2 value for each binned profile with respect to the best-fit model to the observations:

$$\chi^2(\Gamma, b) = \sum_{j=1}^{n} \frac{(P_j^{bin} - P_j^{model})^2}{\sigma_s^2} \tag{5}$$

where P_j^{bin} is the jth of n total points in a binned profile with uncertainty σ_s and P_j^{model} is the value predicted for the jth bin by the best-fit model. We find that only 4% of these χ^2 values are

lower than the χ^2 value for the observed binned profile and thus conclude that a power-law model is a good fit to the data.

Previous studies of young massive clusters (YMCs) like the Arches have shown that they often appear to have extended radial profiles without signs of tidal truncation (Elson et al. 1987; Mackey & Gilmore 2003a,b; McLaughlin & van der Marel 2005). These studies fit these profiles using a model defined by Elson et al. (1987), hereafter referred to as an EFF87 profile model. We fit our profile with this model, adding a constant term b for field contamination:

$$\Sigma(r) = \Sigma_0 \left(1 + \frac{r^2}{a^2}\right)^{-\gamma/2} + b \tag{6}$$

where a is related to the core radius r_c of the cluster:

$$r_c = a \left(2^{2/\gamma} - 1\right)^{1/2} \tag{7}$$

We use the same Bayesian framework as described above, only with this profile as the likelihood function. Since incompleteness prevents our profile from stretching into the core region of the Arches we adopt the core radius r_c determined by Espinoza et al. (2009) of 0.14 ± 0.05 pc in our model. The consequent fit is shown in Figure 11, parameter values in Table 4, and posterior distributions in [APPENDIX 4]. We obtain $\gamma = 2.3 \pm 0.17$, which is consistent with the range and median of values of [2.01 - 3.79] and 2.59 determined from a sample of LMC and SMC YMCs by Mackey & Gilmore (2003a,b). Applying the same χ^2 goodness of fit test above reveals that the EFF87 profile model is not as good of a fit as the single power-law profile model, as 11% of randomly generated profiles are found to have better χ^2 values than the best fit. Given that we have no information about r_c from our sample, we move forward with the single power-law model.

Given the fitted cluster and field kinematic distributions described in § 2.2 we can predict the background contamination b that should be observed in our profile. Given that the mean membership probability of the cluster sample is $\overline{P_m} = 0.916$, then we would expect a field contamination fraction of (1 - $\overline{P_m}$) = 0.084. Assuming these contaminants have a mean membership probability $\overline{P_m}$ themselves, then the background contamination in the profile can be predicted to be:

$$b_{predict} = \frac{(N_{clust} * (1 - \overline{P_m})) * \overline{P_m}}{A_{tot}} \tag{8}$$

where N_{clust} is the number of cluster members and A_{tot} is the observed area. This calculation yields $b_{predict} = 1.7$ stars pc^{-2}, which is consistent with the value of 2.0 ± 1.2 in the best-fit power-law profile. Since P_{member} and thus N_c are dependent on the cluster and field distributions, this indicates that the kinematic population fits are suitable for this study.

3.2.1. Mass Segregation

Evidence for mass segregation in the Arches cluster has been found in the flattening of the mass function toward the cluster center (Figer et al. 1999; Stolte et al. 2002; Espinoza et al. 2009; Habibi et al. 2013) and a shallower radial profile for low-mass stars relative to higher mass stars (Espinoza et al. 2009). However, these results rely on measurements in the dense innermost regions of the cluster (R < 10"), where completeness is lowest for faint low-mass stars due to stellar crowding (Ascenso et al. 2009). We avoid this innermost region, instead covering the less-dense outer regions of the cluster. Following Espinoza et al. (2009), we separate our radial profile as a function of differentially de-reddened magnitude (and thus mass) to qualitatively search for mass segregation. Adopting the single power-law model described above, we find the power-law slope of stars brighter than F153M = 17 mag to be steeper than the slope of stars between F153M = 17 - 20 mag, providing clear evidence for mass segregation and confirming previous findings (Table 3, Figure 12; posteriors in [APPENDIX 4]). We leave the conversion from magnitude to mass to a future paper, as this is complicated by uncertainties in evolutionary tracks and the location of the pre-main sequence in the CMD.

3.2.2. The Search for Tidal Tails

Given the strong gravitational fields near the GC, the Arches cluster is expected to have tidal tails leading and trailing its orbit. Such structures have been observed for globular clusters and have yielded information about the object's orbit and the gravitational potential of the galaxy (i.e. Odenkirchen et al. 2001; Grillmair & Dionatos 2006). Adopting the model of the initial conditions of the Arches from Harfst et al. (2010), the 3D velocity from Clarkson et al. (2012), and assuming a current position 100 pc in front of the GC, Habibi et al. (2014) predict that the Arches should exhibit tidal tails stretching 20 pc (∼500") along the Galactic plane. To search for these structures we compare the radial profiles parallel and perpendicular to the cluster's observed bulk velocity, which falls along the Galactic plane. Tidal tails would be observed as an asymmetry in these profiles, with the parallel profile appearing flatter than the perpendicular profile as it is stretched and sheared by the gravitational tidal field. Using the single power-law model, we find that the parallel profile may have a slightly flatter slope than the perpendicular one, though only at a 1.5σ significance level (Table 3, Figure 12). Posterior distributions are are presented in [APPENDIX 4]. It may that cluster members within a tidal tail structure have $P_{member} < 0.85$, and thus are not considered in the above analysis. To test this, we run the same analysis using all stars with $P_{member} > 0.6$ and come to the same conclusion: no statistically significant tidal tail structures are detected. Deeper observations to obtain a larger sample of cluster members or observations of the cluster at larger radii are needed to confirm or disprove the presence of tidal tails.

3.3. Tidal Radius

Tidally-truncated globular clusters have been found to be well fit by King model profiles:

$$\Sigma(r) = k * \left(\frac{1}{[1 + (r/r_c)^2]^{1/2}} - \frac{1}{[1 + (r_t/r_c)^2]^{1/2}} \right)^2 \quad (9)$$

where k is a normalization constant and r_c and r_t are the core and tidal radii of the cluster, respectively (King 1962). We fit a King model to our profile to constrain the tidal radius of the Arches cluster. We adopt the core radius measured by Espinoza et al. (2009) as a prior for r_c, though our profile provides no additional constraint since incompleteness prevents us from reaching R $\leq$ 0.25 pc. An uninformed prior is used for r_t, and k is calculated for each model such that the integral of the profile over the image yields the total number of cluster members observed after membership probability, completeness, and area corrections. The result of our fit is presented in Table 5 and posterior distributions in [APPENDIX 4]. While we are unable to directly measure the tidal radius, we can place a 3σ lower limit of 2.9 pc. This is surprising given that previous estimates based on the cluster mass and expected galactocentric radius put the tidal radius between 1 and 2.5 pc (Kim et al. 2000; Portegies Zwart et al. 2002; Habibi et al. 2013), yet this is clearly discrepant with our observed profile (Figure 13). We discuss the implications of this in § 4.1.

4. Discussion

4.1. The Arches Cluster: Far Away from the GC or an Inflated Cluster?

Assuming that the Arches cluster has a non-circular orbit, as shown to be likely by Stolte et al. (2008), its tidal radius is set by its closest approach to the GC. At this point the tidal forces felt by the cluster are the strongest, resulting in its smallest possible tidal radius. N-body simulations of clusters in varying tidal fields show that that stars beyond the perigalactic tidal radius are efficiently stripped from the cluster, resulting in a period of increased stellar mass loss (Baumgardt & Makino 2003). While the tidal radius increases and the cluster consequently expands as it moves away from the GC, it expands on relaxation timescales, which for the Arches is significantly larger than its current age ($t_{age} \sim 10^6$ yrs, $t_{rh} \sim 10^7$ yrs). Because of this, the Arches has not yet had sufficient time to re-equilibrate from its closest approach to the GC.

We perform a rough calculation to estimate a lower limit on the closest GC approach distance of the Arches given our constraint on the tidal radius. In a constant tidal field, the tidal radius of a cluster r_t is related to its distance from the galactic center r_g by:

$$r_t = \left(\frac{M_{cl}}{2M_g} \right)^{1/3} r_g \quad (10)$$

where M_{cl} is the cluster mass and M_g is the enclosed galactic mass (Portegies Zwart et al. 2010). As discussed above, for the Arches we assume that $r_g = r_{min}$, the minimum GC approach distance. We adopt a cluster mass of 1.5 x 10^4 $M_\odot$ (Clarkson et al. 2012) and the enclosed mass model in the inner 500 pc of the galaxy by Launhardt et al. (2002), with an updated black hole mass of 4.1 * 10^6 $M_\odot$ (Ghez et al. 2008). A limit of $r_t \geq 2.9$ pc suggests that the Arches could not have passed closer than 180 pc to the GC, much further than previously estimated (Figures 14, 15). This places the cluster on the outskirts of the Central Molecular Zone (CMZ), the highly concentrated structure of molecular gas found in the inner 200 pc of the Galaxy (Morris & Serabyn 1996). A more rigorous constraint on r_{min} requires extensive orbital modeling but is beyond the scope of this paper.

An alternative possibility is that the Arches cluster is inflated beyond its nominal tidal radius, possibly due to cluster expansion due to violent gas loss. Gas loss is expected to occur on dynamical timescales within the first few million years of a cluster's life, destabilizing the cluster and making in vulnerable to dissolution (Lada & Lada 2003). This process and the subsequent formation of an unbound "halo" of stars beyond the tidal radius has been proposed as an explanation for the lack of tidal truncation observed in many YMCs in the LMC and SMC, as these clusters have not completed enough of an orbit to separate from these halos (Elson et al. 1987). However, the Arches presumably has a much smaller galactocentric radius than the vast majority of the LMC and SMC clusters, and so it has completed a larger fraction of an orbit during its lifetime and is exposed to a stronger tidal field (Figure 15). This makes the survival of such an unbound halo difficult, though a high precision kinematic study of the identified cluster members is needed to test this possibility.

Interactions with giant molecular clouds (GMCs) could also inflate the Arches beyond its tidal radius. Tidal heating from these events can completely disrupt a cluster if the interaction is slow and close, limiting cluster lifetimes (Spitzer 1958; Theuns 1991; Gieles et al. 2006). The Arches cluster is thought to be currently interacting with the "−30 km s^{-1}" molecular cloud, creating the Arched Filaments HII complex from which the cluster derives its name. Studies have shown that the ionization properties of the complex can be explained by the Arches cluster if it were located 10-20 pc away (Lang et al. 2001), though the relative geometry between the cluster and cloud structure is likely complex (Lang et al. 2002). Below we estimate the disruption timescale t_{dis} of the Arches cluster from GMCs to assess the likelihood that the cluster has been significantly affected by such interactions within its lifetime.

Starting with a cluster of initial mass M_c, half light radius r_{eff}, and energy $E_0 = -\eta GM^2/(2 * r_h)$ where $r_h = (4/3)r_{eff}$, Gieles et al. (2006) derive an expression for the cluster disruption timescale due to GMCs (their Equation 22):

$$t_{dis} = \frac{3\sigma_{cn}\eta}{8\pi^{(3/2)}gfG}\left(\frac{1}{\Sigma_n \rho_n}\right)\left(\frac{r_h^2}{\overline{r^2}}\right)\frac{M_c}{r_h^3} \tag{11}$$

where $\sigma_{cn} = \sqrt{\sigma_n^2 + \sigma_c^2}$ is the relative velocity dispersion between the GMC population (σ_n) and

cluster population (σ_c), Σ_n is the average surface density of an individual GMC cloud, ρ_n is the mass density of GMCs in the region, $\overline{r^2}$ is the mean-square position of stars in the cluster, and g and f are dimensionless constants accounting for the effect of gravitational focusing and ratio of fractional mass loss ($\Delta M/M_c$) to fractional energy gain ($\Delta E/E_0$) per interaction, respectively. We assume the Arches has an initial tidal radius of 1 pc as previously predicted and a core radius of 0.14 pc (Espinoza et al. 2009), and can thus be described by a King model with $W_0 \approx 4$ ($c \equiv \log(r_t/r_c) = 0.85$). This profile has $(r_h^2/\overline{r^2}) \approx 0.5$ and $\eta \approx 0.4$ (Binney & Tremaine 2008). Figer et al. (1999) measured $r_{eff} = 0.4$ pc for the Arches, and thus $r_h = 0.53$ pc. We adopt $g = 2.5$ and $f = 0.25$ as determined by Gieles et al. (2006) in their simulations, which are derived for the specific case of spherical GMC clouds of mass $M_c = 10^5 M_\odot$ and $\sigma_{cn} = 10$ km s^{-1}.

Several assumptions are required in order to characterize the GMC distribution in the CMZ. Following Kim & Morris (2001), we estimate that the CMZ contains 20 GMCs with a total mass of 5 x 10^7 $M_\odot$ (Oka et al. 1998). Assuming an equal mass distribution among spherically-shaped GMCs with an average radius of 15 pc yields $\Sigma_n = 3.5$ x 10^3 $M_\odot$ pc^{-2}. We model the CMZ as a molecular torus with an inner/outer radius of 10 pc/150 pc and a scale height H(r) = 25(r/150 pc) pc. This scale height is derived by Kim & Morris (2001) using the vertical component of the velocity dispersion at r = 150 pc (25 km s^{-1}) for the X_2 orbit family. Assuming that the GMCs uniformly fill this area results in a GMC mass density of $\rho_n = 42.5$ $M_\odot$ pc^{-3}. We also assume that that $\sigma_{cn} = 20$ km s^{-1}, twice the value derived for GMCs and open clusters in the solar neighborhood, though this value is not well constrained. Plugging these values into Equation 11, we estimate a disruption timescale for the Arches of 6 x 10^7 yrs, ∼25 times larger than its current age of 2.5 x 10^6 yrs. This timescale is about 6 times longer than the predicted cluster lifetimes near the GC due to evaporation in the strong tidal field (Kim et al. 1999, 2000).

Keeping in mind that the assumptions made regarding the properties of the GMC population are vastly oversimplified, this estimate of t_{dis} suggests that it is unlikely for the Arches to be significantly disrupted due to interactions with surrounding GMCs due to its young age. For a more accurate calculation, simulations of this process using non-spherical clouds are required, as GMCs near the GC are known to be sheared due to the strong tidal fields. In addition, the distribution of clouds in the CMZ and σ_{cn} must be better constrained. Obviously the current interaction between the cluster and the Arched Filament cloud could contribute to cluster inflation, although a better understanding of the geometry between the cluster and cloud complex and simulations of this interaction are required to determine its effect.

4.1.1. Possible Consequences for Arches Cluster Formation Scenarios

If the Arches is not inflated and its closest GC approach distance is indeed larger than 180 pc, then this has significant consequences for the different formation scenarios proposed for the cluster. Kruijssen et al. (2014) expand upon the mechanism proposed by Longmore et al. (2013) in which YMCs are formed by the tidal compression of dense molecular gas clouds as they pass near the

GC. The proposed sequence would connect several structures, including the possible YMC progenitor G0.253+0.016 (Longmore 2012) and the Sgr B2 complex, in a direct temporal progression of YMC formation, with the Arches and Quintuplet clusters potentially representing the end product. Previously identified as part of a star-forming elliptical gas ring around the GC (Molinari et al. 2011), Kruijssen et al. (2014) use updated gas kinematics to obtain a new best-fit orbit model for the molecular ring which would place the Arches at a galactocentric radius of just ∼60 pc. This is inconsistent with our limit of 2.9 pc for the tidal radius at closest approach (assuming the cluster is not inflated), suggesting that the Arches is not part of the proposed sequence.

A second formation scenario presented by Stolte et al. (2008, 2014) suggests that the Arches formed in a collision between gas clouds along the X_1 and X_2 orbit families in the Galactic bar, oriented along the bar's major and minor axes, respectively (Binney et al. 1991). Simulations have shown this to be a region of increased star formation (Athanassoula 1992; Kim et al. 2011), perhaps being the source of circum-nuclear star forming rings often observed in barred spiral galaxies (Böker et al. 2008). Simulations of this process in the Milky Way predict increased star formation at a galactocentric radius of ∼200 pc (Kim et al. 2011). This scenario is more consistent with our minimum galactocentric radius constraint for the Arches cluster.

5. Conclusions

We have conducted a multi-epoch photometric and astrometric study of the Arches cluster using the *Hubble Space Telescope* WFC3IR camera at 1.27, 1.39, and 1.53 μm. Using a sophisticated astrometric pipeline we extract individual stellar proper motions to an accuracy $\leq$0.65 mas yr^{-1} down to F153M $\approx$ 20 mag ($\sim 2.5_{\odot}$). Taking advantage of the distinct kinematic properties of the cluster, we use a Bayesian analysis to simultaneously fit the cluster and field kinematic distributions to identify cluster members. This is a substantial improvement over photometrically-determined cluster membership due to the large degree of differential reddening across the field. The field of view in this study is 144 times larger than previous astrometric studies of the Arches cluster, allowing for the identification of 523 cluster members out to cluster radii of ∼3 pc.

Combining the cluster member sample with an extinction map derived from red clump (RC) stars and extensive completeness analysis, we construct the stellar radial density profile for the Arches cluster in the radius range 6.25" < R < 62.5" (0.4 pc < R < 2.5 pc at 8 kpc) down to a differentially de-reddened magnitude of F153M = 20 mag. This profile is well fit by a single power-law model of slope $\Gamma = 2.1 \pm 0.15$ and a constant field contamination $b = 2.0 \pm 1.2$ stars pc^{-1}. We also fit the Arches profile with an Elson et al. (1987; EFF) model and find the Arches to have an EFF power-law slope of $\gamma = 2.3 \pm 0.17$. This is consistent with values determined for YMCs studied in the LMC and SMC by Mackey & Gilmore (2003a,b). Surprisingly, *no evidence of a tidal radius is observed, despite expectations to the contrary.* Using a tidally-truncated King profile as a model, we determine a 3σ lower limit of 2.9 pc for the tidal radius of the Arches cluster.

We additionally examine the Arches cluster profile for evidence of mass segregation and tidal tail structures. We show that the cluster exhibits mass segregation throughout the cluster radii observed from a comparison of the profiles for the brighter (F153M < 17 mag) and fainter (F153M > 17 mag) stars, which reveals the bright star profile to have a steeper power-law slope of $\Gamma = 2.7 \pm 0.3$ compared to $\Gamma = 1.9 \pm 0.1$ for the faint stars. We leave a careful conversion from brightness to mass for a future paper. Similarly, we search for tidal tails by comparing the cluster profile along the direction of the orbit to that perpendicular to the orbit. No significant evidence for tidal tails is found, though these features may be observed with more sensitive observations or a wider field of view.

A tidal radius greater than 2.9 pc suggests that the Arches cluster is either much further from the GC than previously thought or inflated beyond its true tidal radius. Because the cluster's two-body relaxation time is significantly longer than its age ($t_{rh} \approx 10^7$ yrs, $t_{age} \approx 10^6$ yrs), its observed tidal radius is a function of the closest approach distance to the GC. Adopting the Galactic mass model of Launhardt et al. (2002), we constrain the closest approach to be greater than 180 pc, placing the Arches on the outskirts of the Central Molecular Zone. This is consistent with the formation of the Arches at the intersection of the X_1 and X_2 orbits in the Galactic bar but inconsistent with its formation in the molecular cloud ring identified by Molinari et al. (2011).

Alternatively, the cluster could be inflated due to gas loss and the subsequent formation of an unbound halo of stars around the cluster, though the survival of such a structure in the strong tidal field near the GC would be difficult. The cluster may also be inflated through interactions with GMCs, especially given its current apparent interaction with the Arched Filament HII cloud complex. However, the estimated dissipation timescale of 60 Myr makes it unlikely that the Arches has had many significant GMC interactions within its 2.5 Myr lifetime. Detailed modeling of this interaction process in the GC environment as well as a better characterization of the cluster's current interaction with the Arched Filament clouds is needed to fully explore this possibility.

Acknowledgements here

REFERENCES

Allard, F., Homeier, D., & Freytag, B. 2011, in Astronomical Society of the Pacific Conference Series, Vol. 448, 16th Cambridge Workshop on Cool Stars, Stellar Systems, and the Sun, ed. C. Johns-Krull, M. K. Browning, & A. A. West, 91

Anderson, J., & King, I. R. 2006, PSFs, Photometry, and Astronomy for the ACS/WFC, Tech. rep.

Anderson, J., Sarajedini, A., Bedin, L. R., et al. 2008, AJ, 135, 2055

Ascenso, J., Alves, J., & Lago, M. T. V. T. 2009, A&A, 495, 147

Athanassoula, E. 1992, MNRAS, 259, 345

Bastian, N., Covey, K. R., & Meyer, M. R. 2010, ARA&A, 48, 339

Baumgardt, H., & Makino, J. 2003, MNRAS, 340, 227

Binney, J., Gerhard, O. E., Stark, A. A., Bally, J., & Uchida, K. I. 1991, MNRAS, 252, 210

Binney, J., & Tremaine, S. 2008, Galactic Dynamics: Second Edition (Princeton University Press)

Böker, T., Falcón-Barroso, J., Schinnerer, E., Knapen, J. H., & Ryder, S. 2008, AJ, 135, 479

Castellani, V., Chieffi, A., & Straniero, O. 1992, ApJS, 78, 517

Chabrier, G., Hennebelle, P., & Charlot, P. 2014, ArXiv e-prints, arXiv:1409.8466

Clarkson, W., Sahu, K., Anderson, J., et al. 2008, ApJ, 684, 1110

Clarkson, W. I., Ghez, A. M., Morris, M. R., et al. 2012, ApJ, 753, 92

Do, T., Lu, J. R., Ghez, A. M., et al. 2013, ApJ, 764, 154

Elson, R. A. W., Fall, S. M., & Freeman, K. C. 1987, ApJ, 323, 54

Espinoza, P., Selman, F. J., & Melnick, J. 2009, A&A, 501, 563

Feroz, F., Hobson, M. P., & Bridges, M. 2009, MNRAS, 398, 1601

Feroz, F., Hobson, M. P., Cameron, E., & Pettitt, A. N. 2013, ArXiv e-prints, arXiv:1306.2144

Figer, D. F., Kim, S. S., Morris, M., et al. 1999, ApJ, 525, 750

Figer, D. F., Najarro, F., Gilmore, D., et al. 2002, ApJ, 581, 258

Fitzpatrick, E. L. 2004, in Astronomical Society of the Pacific Conference Series, Vol. 309, Astrophysics of Dust, ed. A. N. Witt, G. C. Clayton, & B. T. Draine, 33

Gelman, A., Carlin, J. B., Stern, H. S., Dunson, D. B., & Vehari, V. 2013, Bayesian Data Analysis: Third Edition (Taylor & Francis)

Ghez, A. M., Salim, S., Hornstein, S. D., et al. 2005, ApJ, 620, 744

Ghez, A. M., Salim, S., Weinberg, N. N., et al. 2008, ApJ, 689, 1044

Gieles, M., Portegies Zwart, S. F., Baumgardt, H., et al. 2006, MNRAS, 371, 793

Grillmair, C. J., & Dionatos, O. 2006, ApJ, 641, L37

Habibi, M., Stolte, A., Brandner, W., Hußmann, B., & Motohara, K. 2013, A&A, 556, A26

Habibi, M., Stolte, A., & Harfst, S. 2014, A&A, 566, A6

Harfst, S., Portegies Zwart, S., & Stolte, A. 2010, MNRAS, 409, 628

Howard, C. D., Rich, R. M., Clarkson, W., et al. 2009, ApJ, 702, L153

Jones, B. F., & Walker, M. F. 1988, AJ, 95, 1755

Kim, S. S., Figer, D. F., Kudritzki, R. P., & Najarro, F. 2006, ApJL, 653, L113

Kim, S. S., Figer, D. F., Lee, H. M., & Morris, M. 2000, ApJ, 545, 301

Kim, S. S., & Morris, M. 2001, ApJ, 554, 1059

Kim, S. S., Morris, M., & Lee, H. M. 1999, ApJ, 525, 228

Kim, S. S., Saitoh, T. R., Jeon, M., et al. 2011, ApJ, 735, L11

King, I. 1962, AJ, 67, 471

Kozhurina-Platais, V., Girard, T. M., Platais, I., et al. 1995, AJ, 109, 672

Kruijssen, J. M. D., Dale, J. E., & Longmore, S. N. 2014, ArXiv e-prints, arXiv:1412.0664

Kunder, A., Koch, A., Rich, R. M., et al. 2012, AJ, 143, 57

Lada, C. J., & Lada, E. A. 2003, ARA&A, 41, 57

Lang, C. C., Goss, W. M., & Morris, M. 2001, AJ, 121, 2681

—. 2002, AJ, 124, 2677

Larson, R. B. 2005, MNRAS, 359, 211

Launhardt, R., Zylka, R., & Mezger, P. G. 2002, A&A, 384, 112

Longmore, S. N. 2012, ArXiv e-prints, arXiv:1211.1223

Longmore, S. N., Kruijssen, J. M. D., Bally, J., et al. 2013, MNRAS, 433, L15

Mackey, A. D., & Gilmore, G. F. 2003a, MNRAS, 338, 120

—. 2003b, MNRAS, 338, 85

Martins, F., Hillier, D. J., Paumard, T., et al. 2008, A&A, 478, 219

Mauerhan, J. C., Cotera, A., Dong, H., et al. 2010, ApJ, 725, 188

McLaughlin, D. E., & van der Marel, R. P. 2005, ApJS, 161, 304

Meynet, G., & Maeder, A. 2000, A&A, 361, 101

Mishenina, T. V., Bienaymé, O., Gorbaneva, T. I., et al. 2006, A&A, 456, 1109

Molinari, S., Bally, J., Noriega-Crespo, A., et al. 2011, ApJ, 735, L33

Morris, M. 1993, ApJ, 408, 496

Morris, M., & Serabyn, E. 1996, ARA&A, 34, 645

Najarro, F., Figer, D. F., Hillier, D. J., & Kudritzki, R. P. 2004, ApJL, 611, L105

Nishiyama, S., Tamura, M., Hatano, H., et al. 2009, ApJ, 696, 1407

Odenkirchen, M., Grebel, E. K., Rockosi, C. M., et al. 2001, ApJ, 548, L165

Oka, T., Hasegawa, T., Sato, F., Tsuboi, M., & Miyazaki, A. 1998, ApJS, 118, 455

Paczynski, B., & Stanek, K. Z. 1998, ApJ, 494, L219

Portegies Zwart, S. F., Makino, J., McMillan, S. L. W., & Hut, P. 2002, ApJ, 565, 265

Portegies Zwart, S. F., McMillan, S. L. W., & Gieles, M. 2010, ARA&A, 48, 431

Rieke, G. H., Rieke, M. J., & Paul, A. E. 1989, ApJ, 336, 752

Salpeter, E. E. 1955, ApJ, 121, 161

Sanders, W. L. 1971, A&A, 15, 368

Schödel, R., Najarro, F., Muzic, K., & Eckart, A. 2010, A&A, 511, A18

Siess, L., Dufour, E., & Forestini, M. 2000, A&A, 358, 593

Spitzer, Jr., L. 1958, ApJ, 127, 17

Stanek, K. Z., Kaluzny, J., Wysocka, A., & Thompson, I. 2000, Acta Astron., 50, 191

Stetson, P. B. 1987, PASP, 99, 191

Stolte, A., Brandner, W., Grebel, E. K., Lenzen, R., & Lagrange, A.-M. 2005, ApJL, 628, L113

Stolte, A., Ghez, A. M., Morris, M., et al. 2008, ApJ, 675, 1278

Stolte, A., Grebel, E. K., Brandner, W., & Figer, D. F. 2002, A&A, 394, 459

Stolte, A., Morris, M., Ghez, A., et al. 2011, in Stellar Clusters Associations: A RIA Workshop on Gaia, 304–308

Stolte, A., Morris, M. R., Ghez, A. M., et al. 2010, ApJ, 718, 810

Stolte, A., Hußmann, B., Morris, M. R., et al. 2014, ApJ, 789, 115

Sumi, T. 2004, MNRAS, 349, 193

Theuns, T. 1991, Mem. Soc. Astron. Italiana, 62, 909

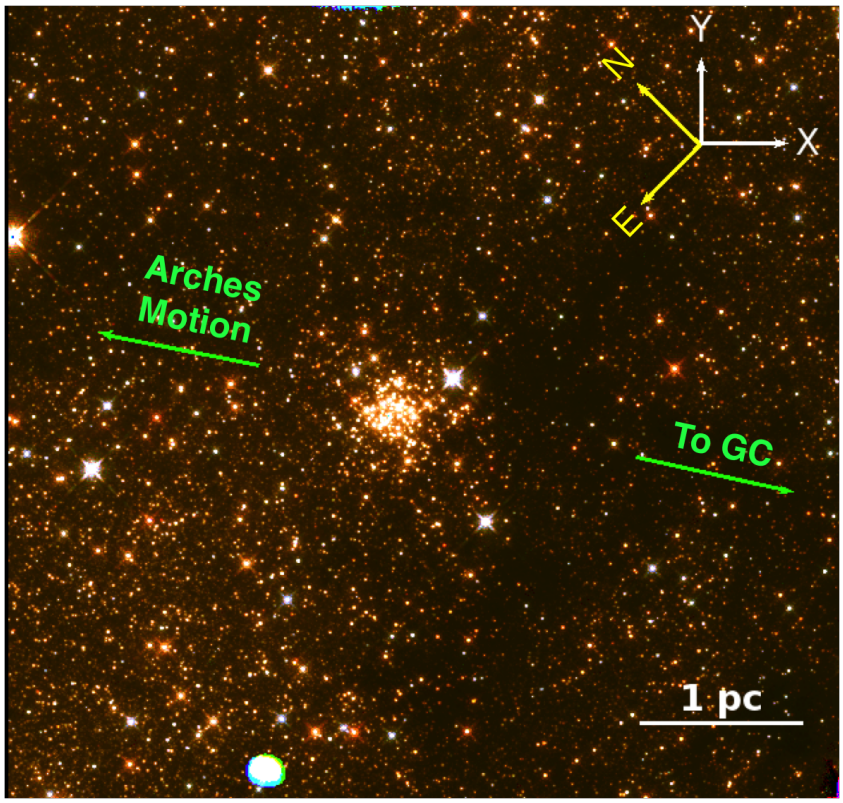

Fig. 1.— Three color image of the Arches Cluster, with F127M = blue, F139M = green, and F153M = red. Significant differential extinction is apparent from the changing density of the field stars. The hole in the left side of the image is due to a defect in the WFC3IR chip. The proper motion of the cluster (labeled with green arrow) is very nearly parallel to the galactic plane.

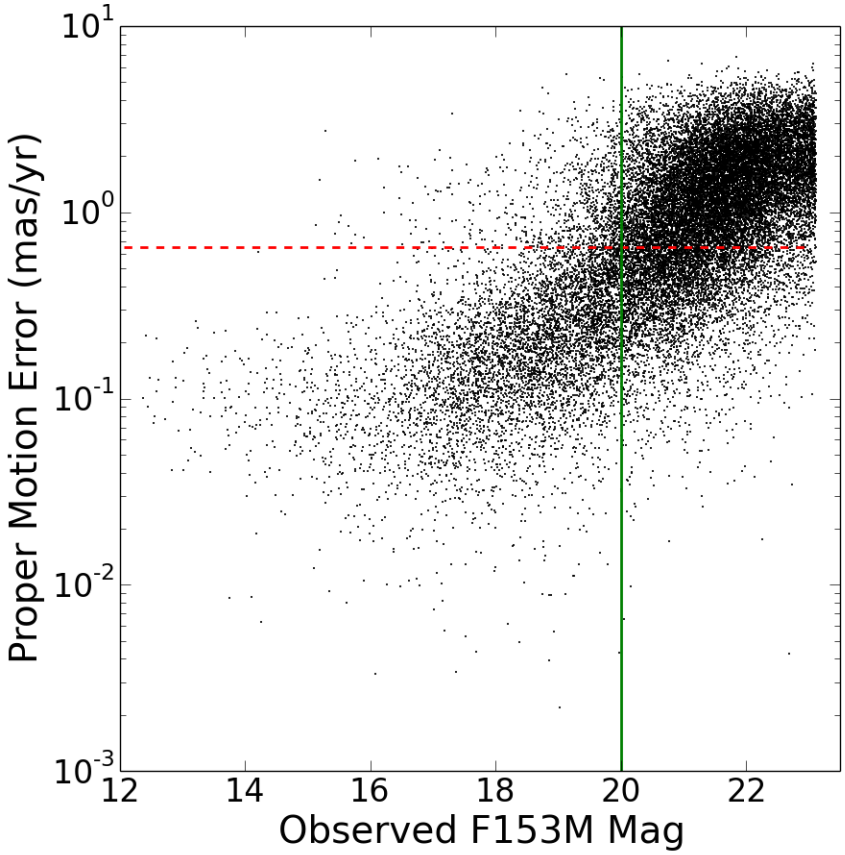

Fig. 2.— Proper Motion error vs. F153M magnitude. The red line marks our proper motion error cut of 0.65 mas yr^{-1}. Only stars below this cut are included in our analysis. The green line corresponds to F153M = 20 mag, which corresponds to 2.5 $M_{\odot}$ at the approximate distance and average reddening of the Arches cluster.

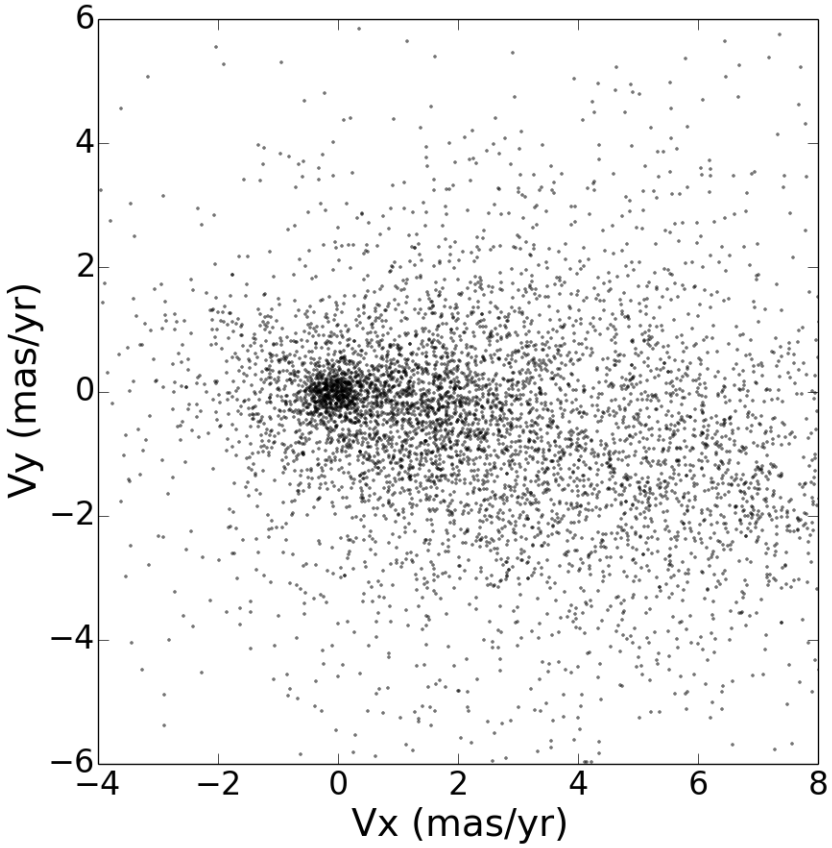

Fig. 3.— Vector point diagram of the ∼4500 stars included in our analysis in the bulk reference frame of the cluster. Cluster members appear as a distinct clump of stars at $(v_x, v_y) = (0, 0)$.

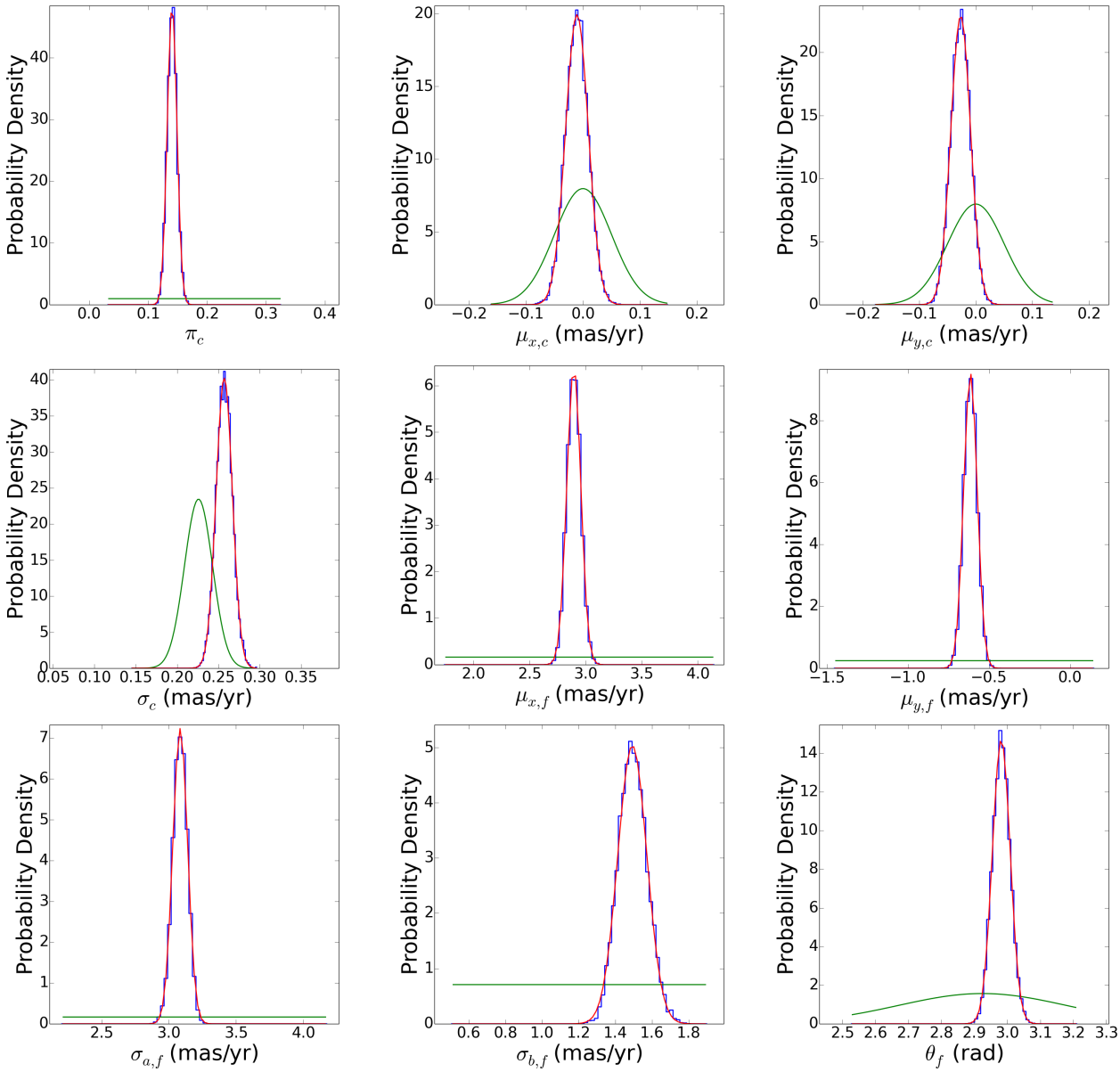

Fig. 4.— One-dimensional posterior distributions for the free parameters in our cluster and field population model described in Table 2. The blue line shows the posterior distribution, the red line is a gaussian fit to the distribution, and the green line describes the input prior. Best fit values and uncertainties are taken from the mean and standard deviation of the gaussian fits.

Table 1. HST WFC3IR Observations

Date	Filter	N_{images}	Total Exp. Time (s)	Depth (mag)	Pos Error (mas)[a]	Phot Error (mag)[a]
2010.6150	F127M	12	7811	23.63	0.60	0.02
2010.6148	F139M	10	3490	23.29	0.90	0.03
2010.6043	F153M	21	7329	23.31	0.88	0.05
2011.6829	F153M	21	7329	23.32	0.88	0.05
2010.6156	F153M	21	7329	23.31	0.88	0.05

[a]Median value at mag = 20 in respective filter

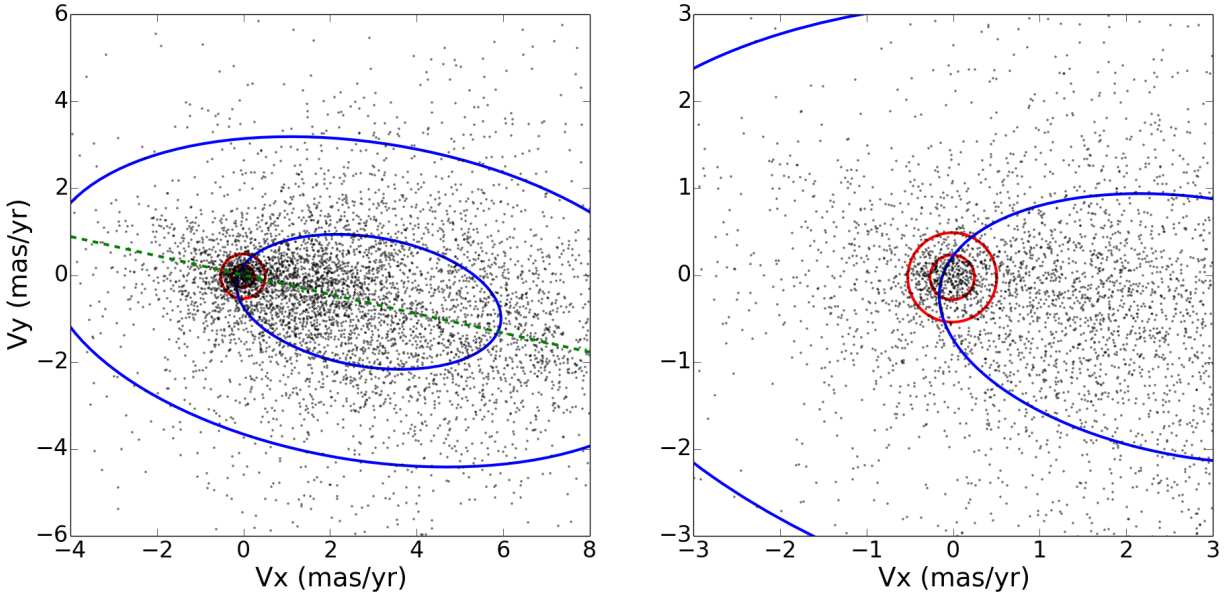

Fig. 5.— Vector point diagram of all stars included in our analysis with the fitted 1- and 2σ cluster and field populations overlaid in red and blue, respectively. The left plot shows the wide distribution of field velocities stretched along the galactic plane, indicated by the green dotted line. The right plot is focused view of the cluster, readily apparent as a tight clump of stars moving with a common motion relative to the field population.

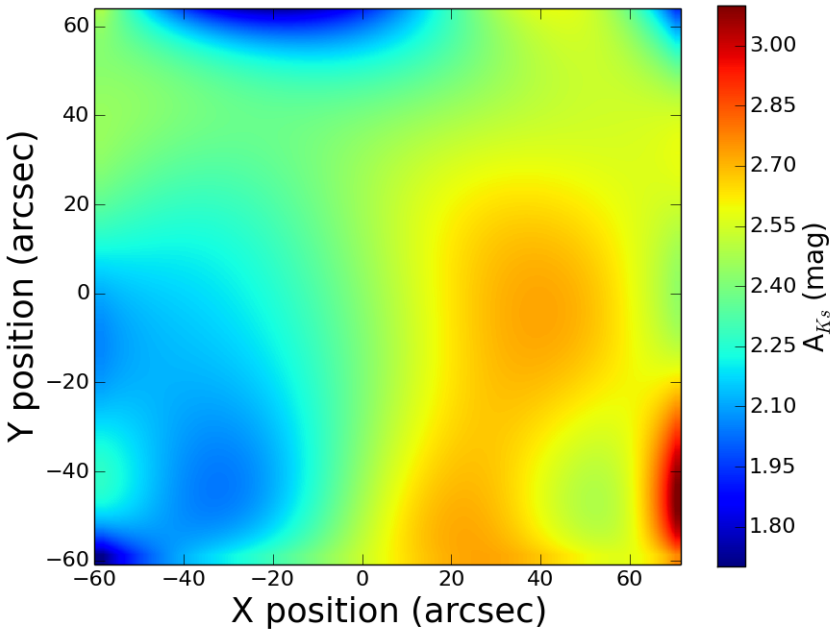

Fig. 6.— An extinction map (in terms of A_{Ks}) of the field created via the spatial interpolation of the RC extinction values as described in the text. The Nishiyama et al. (2009) IR reddening law is used to calculate A_λ at different wavelengths. The cluster is centered at (0, 0) exhibits an average reddening of $A_{Ks} = 2.4$ mag. Plot is oriented in same manner as Figure 1.

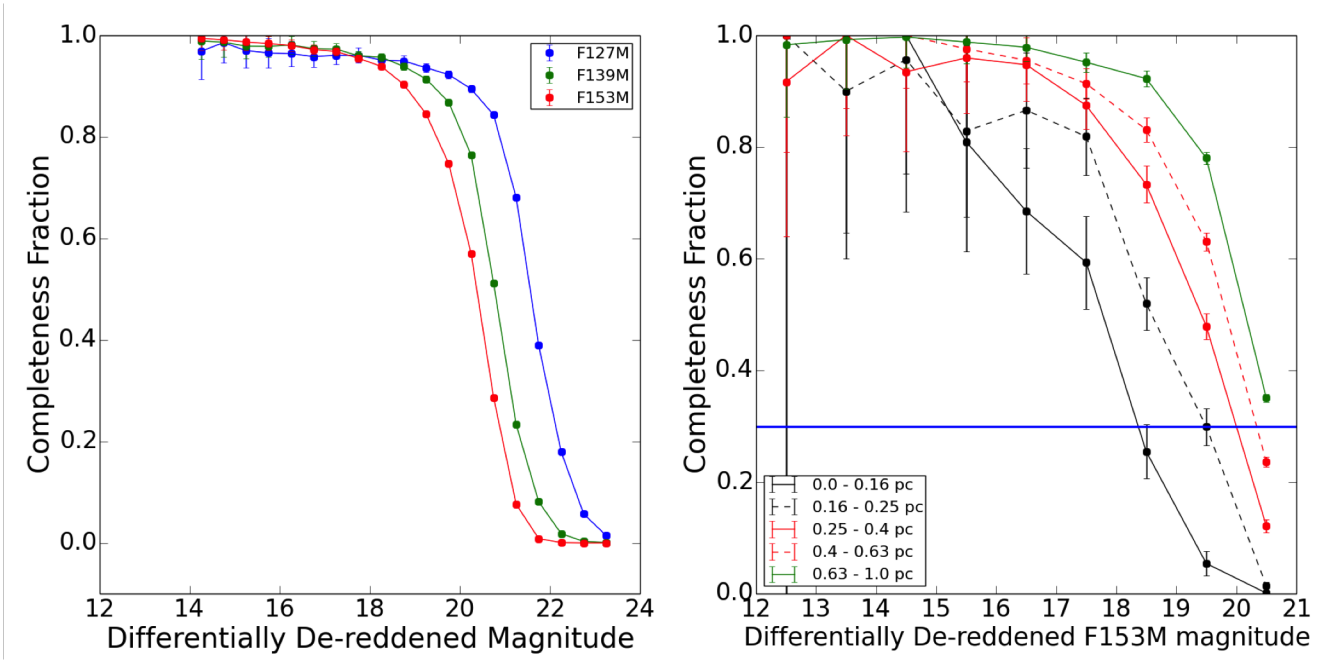

Fig. 7.— Completeness as a function of observed magnitude and radius. *Left*: Completeness as a function of differentially de-reddened magnitude (A_{Ks} = 2.4 mag) for the F127M, F139M, and F153M filters. These completeness values are calculated over the entire field. *Right*: Same as left plot, but only for F153M and separated into different radius bins. The blue line marks a minimum completeness fraction of 30%, which is obtained at R > 0.25 pc for all stars with F153M ≤ 20. This sets the faint magnitude limits for our radial profile.

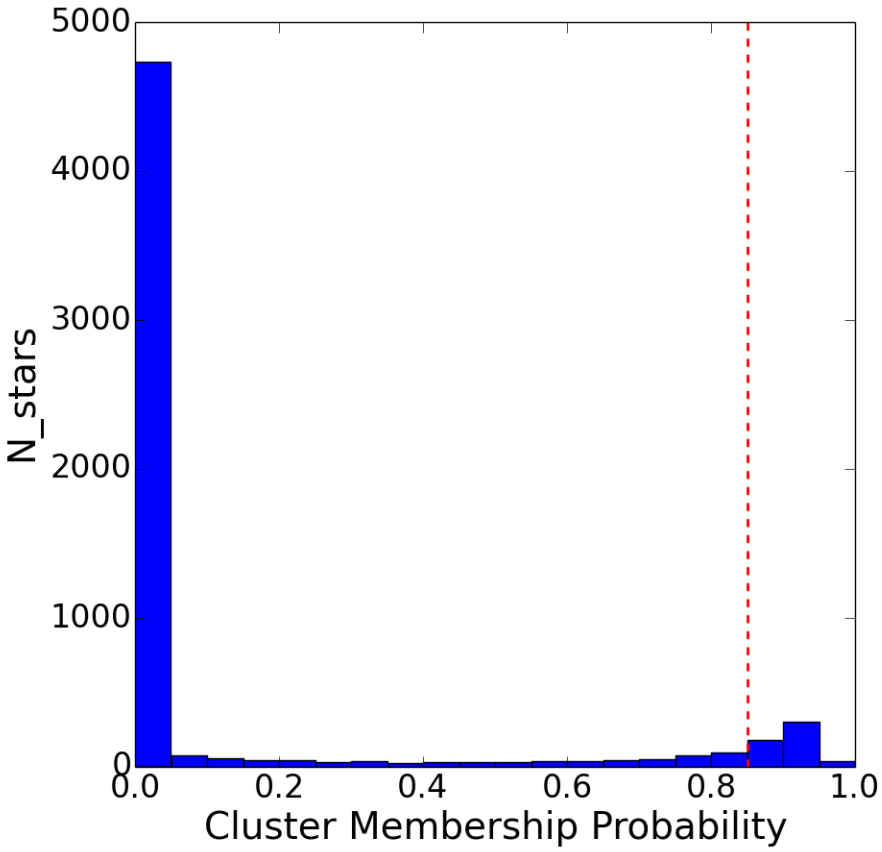

Fig. 8.— A histogram of the calculated membership probabilities for the observed stars. All objects with $P_{cluster} \geq 0.85$ (red line) are identified as cluster members. Of ∼4500 stars analyzed, 523 meet this criteria.

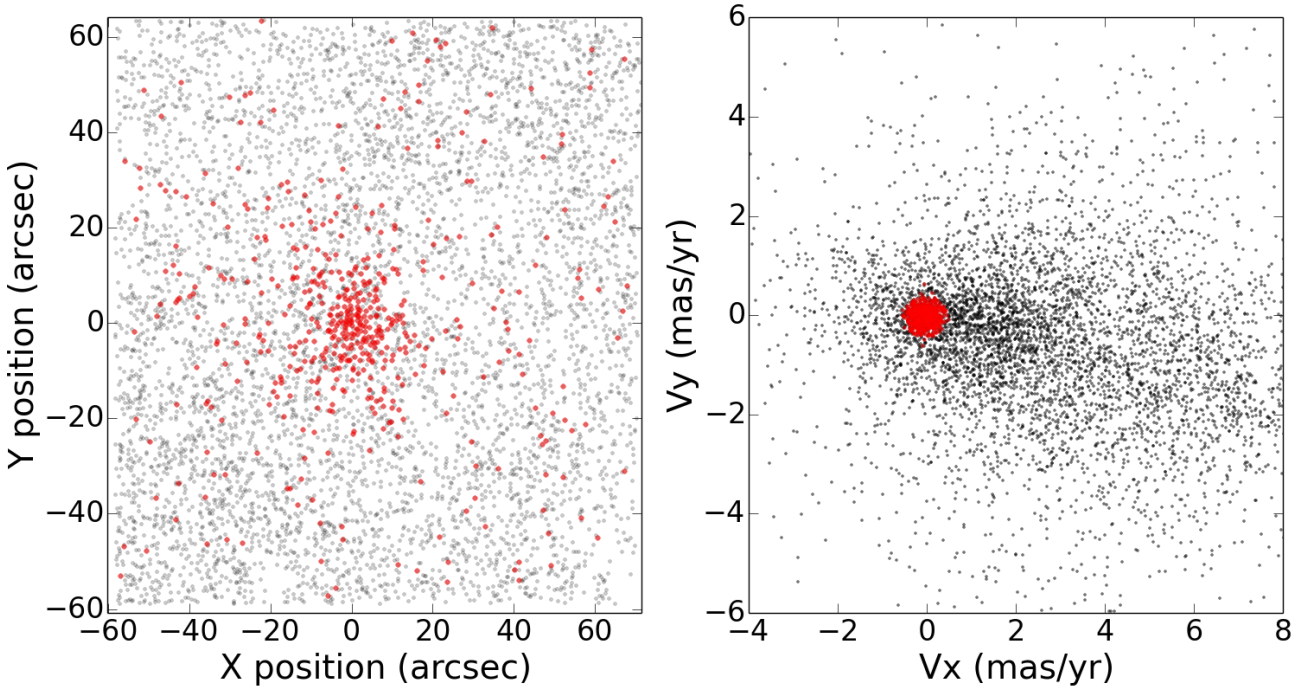

Fig. 9.— The spatial (left) and kinematic (right) positions of identified cluster members, marked as red points. The spatial positions are plotted in arcseconds relative to the cluster center.

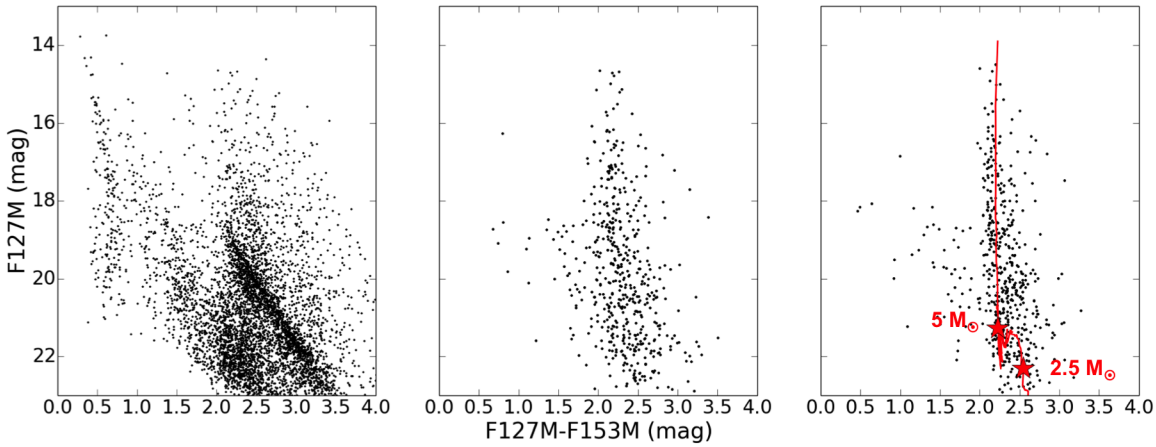

Fig. 10.— The F127M vs. [F127M - F153M] color-magnitude diagram for the observed field (left), identified cluster members (middle), and cluster members after being differentially de-reddened using the extinction map ($A_{Ks} = 2.4$ mag, left). The reddening correction noticeably tightens the color dispersion and blue edge of the population. The differentially de-reddened CMD agrees well with a theoretical 2.5 Myr cluster isochrone also with $A_{Ks} = 2.4$ mag, overlaid in red. The locations of 2.5 and 5 $M_\odot$ stars are shown by the red stars. The isochrone is created using the pre-main sequence evolutionary models of Siess et al. (2000) for $M < 7$ $M_\odot$ and the main sequence models with rotation of Meynet & Maeder (2000) for $M > 9$ $M_\odot$, with an interpolation between the models over the missing mass range.

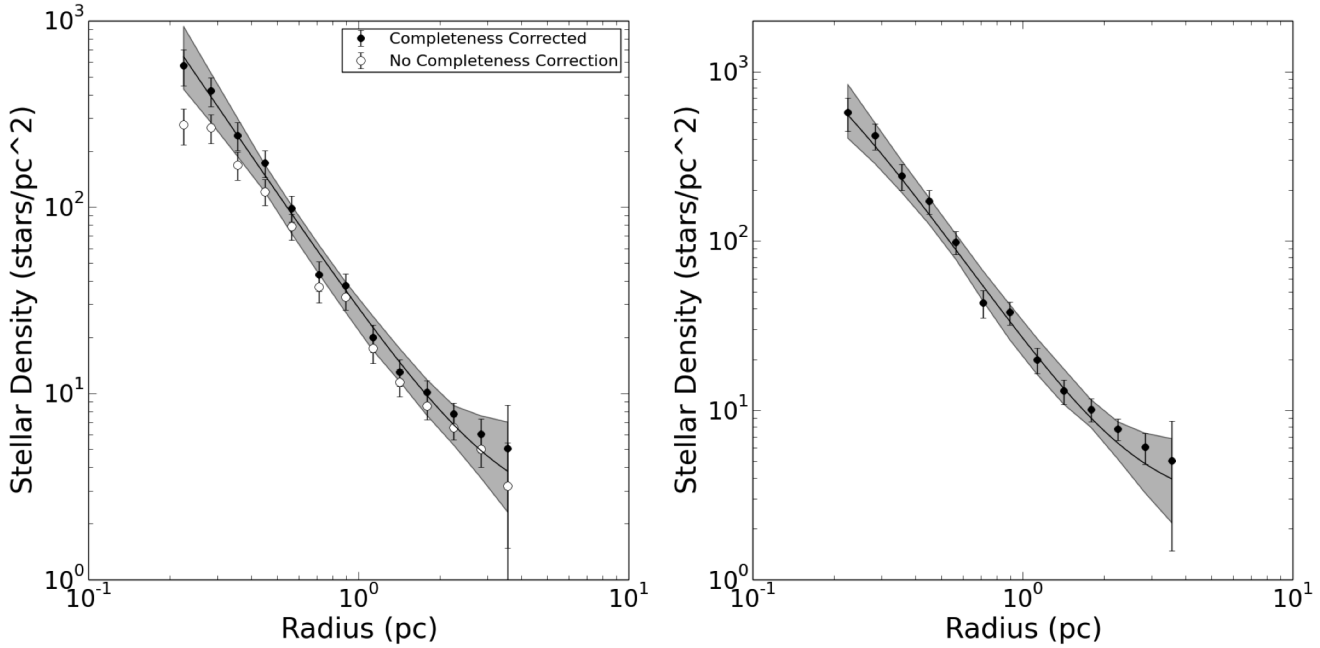

Fig. 11.— The radial profile of the Arches Cluster. *Left*: The best-fit power law model as described in the text and Table 3. The black line represents the fit, black open points the binned profile before completeness correction, and the black solid points the binned profile after completeness correction. Uncertainty in the fit is captured by the gray filled region, which spans the most extreme profiles sampled in 1000 randomly-drawn profile parameters from the joint posterior distribution. The flattening at large radii is caused by field contamination, which matches what would be expected given our 85% membership probability cut. *Right*: Same as left, but with the best-fit EFF87 profile model. Best-fit parameters are provided in Table 4.

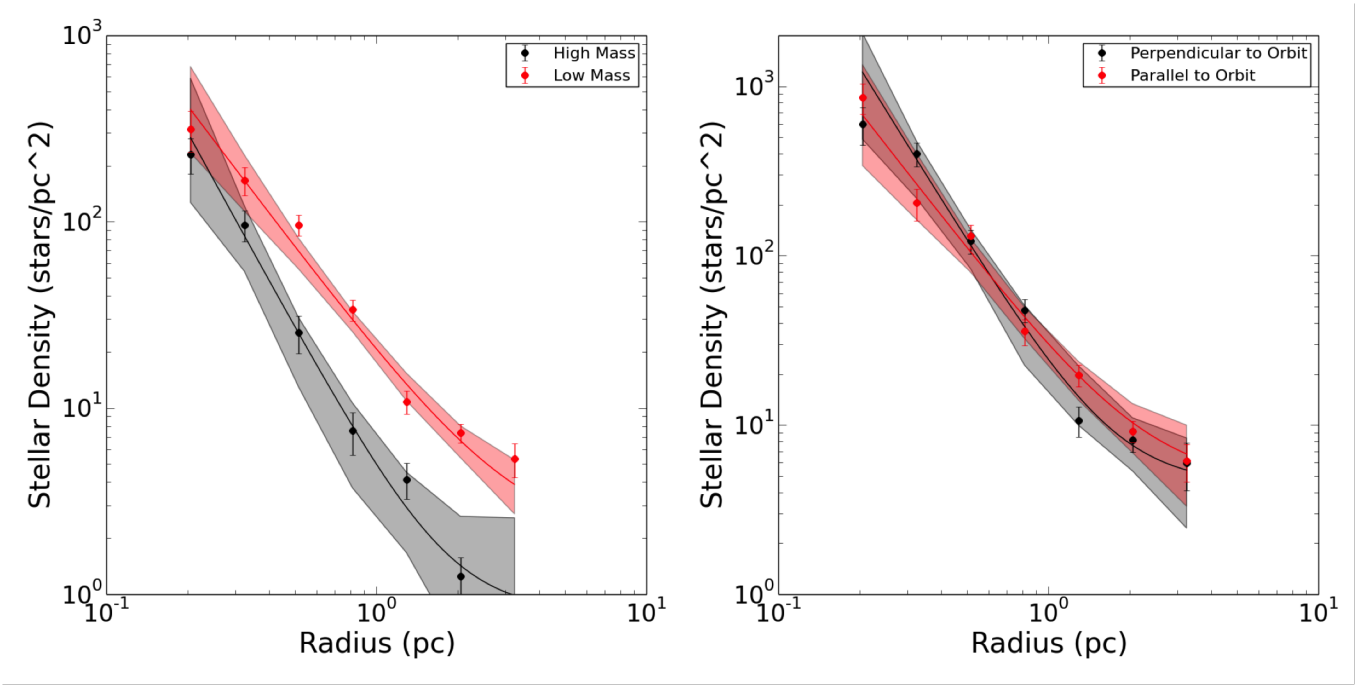

Fig. 12.— Examination of mass segregation (left) and tidal tails (right) in the profile of the Arches cluster. Clear evidence for mass segregation is found in the steepening of the profile for high-mass stars (black; F153M $\leq$ 17 mag) compared to low-mass stars (red; F153M $>$ 17 mag). The solid lines show the power law fits while the data points show the completeness-corrected binned profiles. No statistically significant evidence for tidal tails is found in a comparison of the profile parallel (red) and perpendicular (black) to the cluster's orbit. Model uncertainties are shown in the same manner as Figure 11, and best-fit parameter values are presented in Table 3.

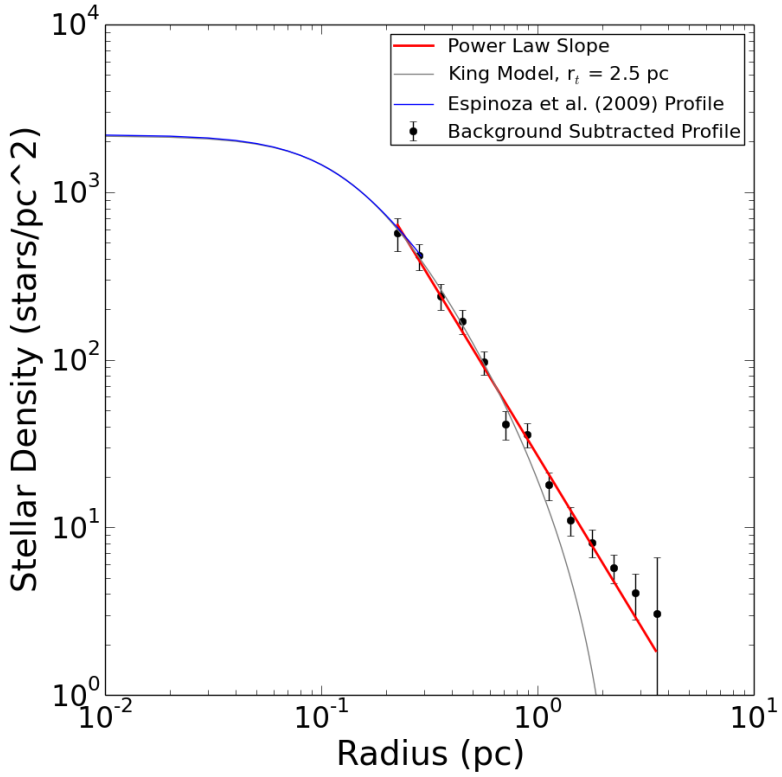

Fig. 13.— Our background-subtracted profile compared to a King profile with tidal radius $r_t = 2.5$ pc, previously proposed to be the upper limit for the tidal radius of the Arches (Habibi et al. 2013). Included are the best-fit power law slope (see § 3.2) and profile for the inner 0.4 pc measured by Espinoza et al. (2009). The Espinoza et al. (2009) profile has been scaled upward to account for the increased depth of our profile ($\sim$2.5 $M_\odot$ vs. $\sim$10 $M_\odot$). The King profile model shown here is clearly discrepant with our results. We place a 3σ lower limit of 2.9 pc on the tidal radius of the Arches cluster.

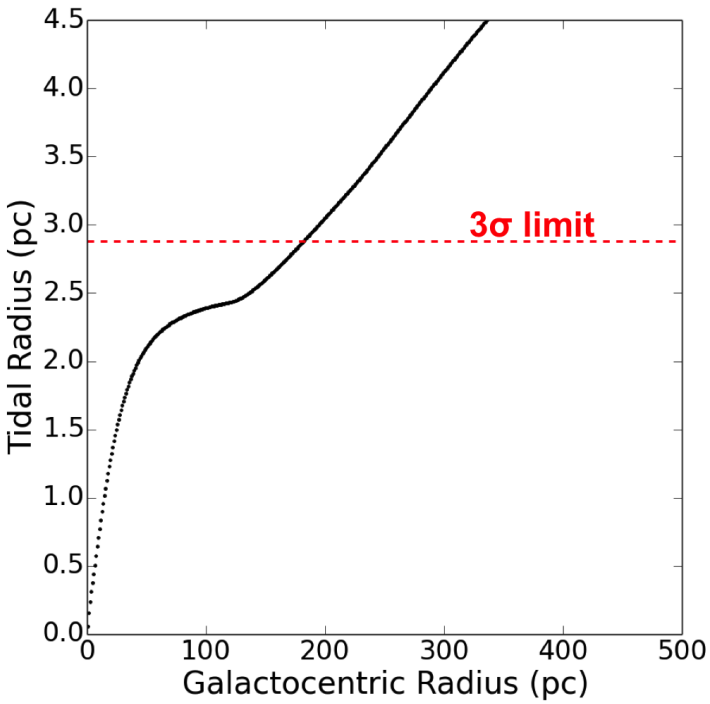

Fig. 14.— Tidal radius as a function of minimum galacticocentric radius for the Arches cluster, adopting a cluster mass of 1.5 x 10^4 (Clarkson et al. 2012) and a mass model inner galaxy by Launhardt et al. (2002). The red line shows $r_t = 2.9$ pc, the 3σ lower limit on the tidal radius from this study, which corresponds to a minimum galactocentric distance of 180 pc.

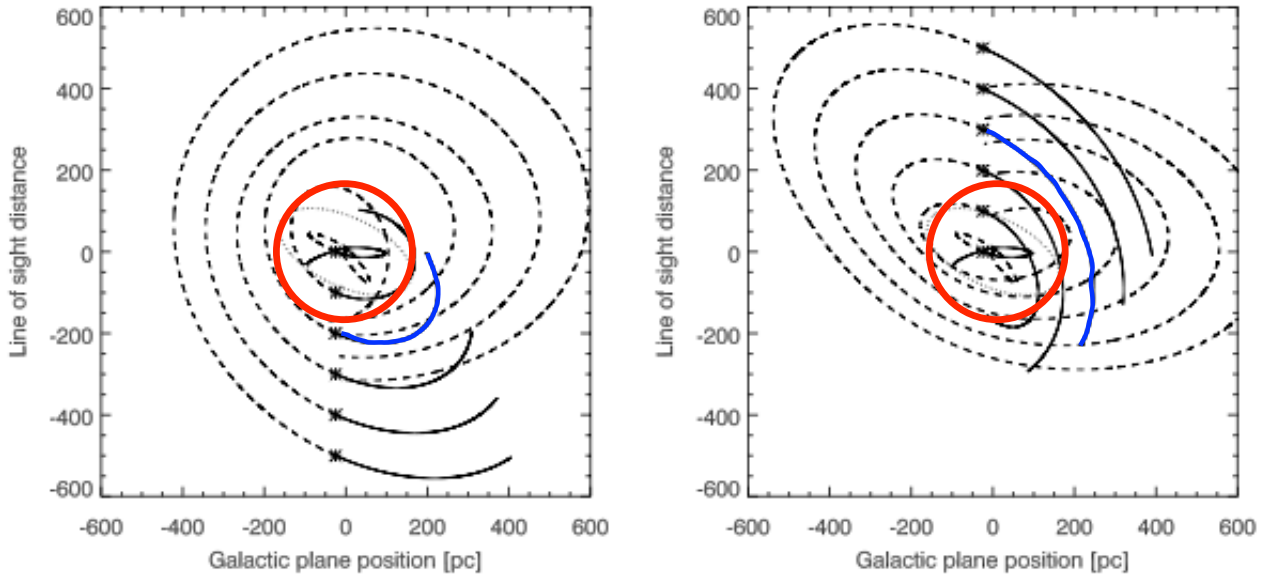

Fig. 15.— The constraint of $r_{min} > 180$ pc (red circle) applied to selected possible prograde (left) and retrograde (right) orbits for the Arches cluster by Stolte et al. (2008). Any orbit that enters this limit would create a tidal radius less than 2.9 pc, inconsistent with our measured profile. The blue lines highlight examples of orbits compatible with this constraint. This figure is adapted from Figure 8 of Stolte et al. (2008).

Table 2. Cluster and Field Population Model: Free Parameters, Priors, and Results

Parameter	Description	Prior[a,b]	Source	Result
π_c	Fraction of stars in cluster	Uniform(0, 1)	–	0.17 ± 0.01
$\mu_{x,c}$	Cluster X velocity (mas yr^{-1})[c]	Gaussian(0, 0.05)	–	-0.12 ± 0.02
$\mu_{y,c}$	Cluster Y velocity (mas yr^{-1})[c]	Gaussian(0, 0.05)	–	-0.004 ± 0.02
$\mu_{x,f}$	Field X velocity (mas yr^{-1})[c]	Uniform(0, 6)	–	2.49 ± 0.07
$\mu_{y,f}$	Field Y velocity (mas yr^{-1})[c]	Uniform(-2, 4)	–	-0.54 ± 0.05
σ_c	Kinematic dispersion of cluster (mas yr^{-1})	Gaussian(0.226, 0.017)	[d]	0.26 ± 0.01
$\sigma_{a,f}$	Kinematic dispersion of field semi-major axis (mas yr^{-1})	Gaussian(2.55, 0.29)	[d]	3.08 ± 0.07
$\sigma_{b,f}$	Kinematic dispersion of field semi-minor axis (mas yr^{-1})	Gaussian(1.66, 0.197)	[d]	1.52 ± 0.10
θ_f	Angle between $\sigma_{a,f}$ and image X axis (rad)	Gaussian(2.924, 0.255)	[d]	2.98 ± 0.05

[a]Uniform distributions presented as Uniform(min, max), where min and max are bounds of the distribution

[b]Gaussian distributions presented as Gaussian(μ, σ), where μ is the mean and σ is the standard deviation

[c]In rest frame of cluster

[d]Clarkson et al. (2012)

Table 3. Power-Law Profile Fit Results

	Γ Power-law slope	b (stars / pc^2) Field Contamination	A (stars / pc^2) Normalization Constant
Full Cluster	2.1 ± 0.15	2.0 ± 1.2	26.8 ± 3.4
Mass Separation: High Mass[a]	2.7 ± 0.3	0.8 ± 0.5	4.2 ± 1.4
Low Mass[b]	1.9 ± 0.1	1.8 ± 0.5	18.9 ± 1.3
Directional Profile: Parallel[c]	2.1 ± 0.2	4.5 ± 2.7	25.7 ± 5.4
Perpendicular[c]	2.6 ± 0.2	4.5 ± 1.5	20.0 ± 4.2
Prior[d]	Uniform(0.5, 4.5)	Uniform(0,8)	—

[a]MASS LIMIT

[b]MASS LIMIT

[c]Relative to Arches cluster orbital motion

[d]Uniform distributions presented as Uniform(min, max), where min and max are bounds of the distribution

Table 4. EFF87 Profile Fit Results[a]

Parameter	Description	Prior[b]	Result
γ	Power-law Slope	Uniform(0.5, 4.5)	2.3 ± 0.17
b	Field Contamination (stars / pc^2)	Uniform(0, 8)	2.6 ± 1.2
a	EFF87 core radius (pc)	—	0.13 ± 0.03
Σ_0	Normalization Constant	—	2820 ± 1082

[a]Profile model defined in Elson et al. (1987)

[b]Uniform distributions presented as Uniform(min, max), where min and max are bounds of the distribution

Table 5. King Profile Fit Results[a]

Parameter	Description	Prior[b]	Result
r_t	Tidal Radius (pc)	Uniform(1, 15)	2.9[c]
r_c	Core Radius (pc)	Gaussian(0.14, 0.05)[d]	0.12 ± 0.03
b	Field Contamination (stars / pc^2)	Uniform(0,8)	2.7 ± 1.0
k	Normalization Constant	—	2223 ± 827

[a]Profile model defined in King (1962)

[b]Uniform distributions presented as Uniform(min, max), where min and max are bounds of the distribution. Gaussian distributions presented as Gaussian(mean, standard deviation)

[c]3σ lower limit

[d]Source: Espinoza et al. (2009)

Appendix 1: WFC3IR Measurements and Proper Motions

In this appendix we describe the methods used to extract high precision astrometry, photometry, and proper motions from the WFC3IR observations. Stars are first detected and measured using the FORTRAN program *img2xym_wfc3ir_stdpsf* developed by Jay Anderson. Similar to the code *img2xym_WFC.09x10* documented in Anderson & King (2006), this performs PSF-fitting measurements using a library of spatially-variable PSF models for the WFC3IR camera. This library contains a 3x3 grid of PSFs that spans the camera's field, where the PSF at any point can be derived from a spatial interpolation of these models. Since this routine operates on only one image at a time in a single pass, it is not designed to deal with overlapping stars. It reduces each star as if it is the only contribution to the 5x5 pixels centered on its brightest pixel.

Each image is run through this program twice. The first iteration only extracts the bright high S/N stars in the field (∼400 stars per image), simultaneously measuring the residuals between the observed PSF and the library PSF. New image-specific PSF models are created in order to minimize these residuals and make them uniform across the field. The second iteration then uses the modified PSF library to accurately measure both bright and faint sources, producing a star list with fluxes and positions for ∼13,000 sources in each image extending down to F127M = 22.45 mag, F139M = 22.09 mag, and F153M = 21.71 mag. A small number of stars (∼200) with F153M ≤∼15 are saturated and are thus measured using the outer part of the PSF.

Next, we cross-identify stars from each exposure with a master list for the filter/epoch set, initially taken to be the first image in the set. Common stars found in at least 75% of the images are used to transform positions from the distortion-corrected frame of each exposure into the master list reference frame using general 6-parameter linear transformations. This gives ∼N observations for each star, where N is the number of images in the filter/epoch set, which allows us to find a robust average position and flux. These averaged measurements produce an overall star catalog for the filter/epoch. We then adopt these catalogs as the new reference-frame positions and repeat the procedure, improving the transformations. The improvement in the second iteration is considerable, decreasing astrometric residuals by nearly a factor of 2. Finally, the new star catalogs for each filter/epoch are then transformed to an overall common astrometric reference frame (arbitrarily chosen to be 2010 F153M). This produces what we will call the "one-pass" catalogs, because they are limited to the stars which can be detected in a single image.

In principle, we could continue our analysis of the Arches Cluster using the one-pass catalogs. However, by stacking the images for each filter/epoch we significantly increase the detection depth, important because signal from otherwise undetected faint stars can be mistakenly associated with brighter stars and introduce biases in the measurements. Using the transformations and PSF models developed above, we use the program *KS2*, which is a generalization of the software program developed to reduce the Globular-Cluster Treasury Program (Anderson et al. 2008), which iteratively finds and measures stars in multiple _flt exposures simultaneously. This multiple-finding strategy increases the number of stars detected to ∼50,000 per filter (nearly five times as many as

the one-pass analysis), reaching F127M = 23.63 mag, F139M = 23.29 mag, and F153M = 23.31 mag as noted in § 2.1. To ensure the accuracy of our transformation we again combine the individual star lists into star catalogs for each filter/epoch and re-align to the common astrometric reference frame using a first-order bi-variate polynomial (see Ghez et al. 2005 and references therein). Higher order fits were tried but were found to introduce artificial structure in the astrometry. Astrometric and photometric errors as a function of magnitude are presented in Figure 16.

The *KS2* code returns a final star catalog with the root-mean-square (RMS) errors for the astrometry and photometry for each star in the filter/epoch, though theoretically the errors should be quantified by the error on the mean (RMS error / $\sqrt{N_{obs}}$, where N_{obs} is the number of images in the filter/epoch). To test this, we compare the *KS2* errors to quantities measured across the F153M epochs that are directly caused by these errors: the standard deviation of the magnitude of each star (assuming no stellar variability) and the RMS residuals between the measured position and position predicted by the star's proper motion. This comparison reveals the error on the mean to better capture the astrometric errors and the RMS error to better capture the photometric errors, and so we adopt these for the individual star measurements moving forward (Figure 17). This choice does not significantly affect the proper motion errors described below, which are dominated by position residuals rather than the astrometric errors themselves.

Photometry is calibrated to the standard Vega magnitude system by deriving the filter-dependent offset between *KS2* magnitudes and 0.4" aperture photometry magnitudes. Aperture photometry is performed using *DAOPHOT* (Stetson 1987) on the drizzled image for each epoch/filter. This offset is then combined with the appropriate 0.4" zeropoint derived for the WFC3IR camera (see § 2.1 for reference) to determine the overall zeropoint for the *KS2* observations. For stars with F153M $\leq$ 20 (consistent with our proper motion precision cut, § 2.1), the median F153M astrometric and photometric errors are 0.34 mas and 0.018 mags, respectively, with evidence of higher errors in regions of increased stellar density (Figure 18). Within this sample the median F127M and F139 photometric errors are 0.033 mag and 0.025 mag, respectively.

Proper motions are derived independently for the X and Y directions (in the image coordinate system) using a linear fit to the change in position over the F153M epochs:

$$x = x_0 + v_x(t - t_0) \qquad (1)$$
$$y = y_0 + v_y(t - t_0)$$

where t_0 is the astrometric error-weighted average time of observations, (v_x, v_y) are the X and Y proper motions, and (x_0, y_0) and (x, y) are the star positions at t_0 and t, respectively. To test the validity of these errors, we apply the derived proper motions to their respective stars and examine the residuals between the predicted and the observed positions. The distributions of the X and Y position residuals are approximately Gaussian, though more power is present in the wings than expected (Figure 19). This is a consequence of stellar crowding distorting our measurements, as

these wings are dominated by faint stars (F153M $<$ 20 mag) which are more prone to this effect. Given the high stellar density of our field this is not unexpected. This is also seen in the distribution of χ^2 values for the proper motion fits, which has a larger number of high values than expected for a χ^2 distribution with 1 degree of freedom (appropriate for constraining 2 parameters with 3 measurements).

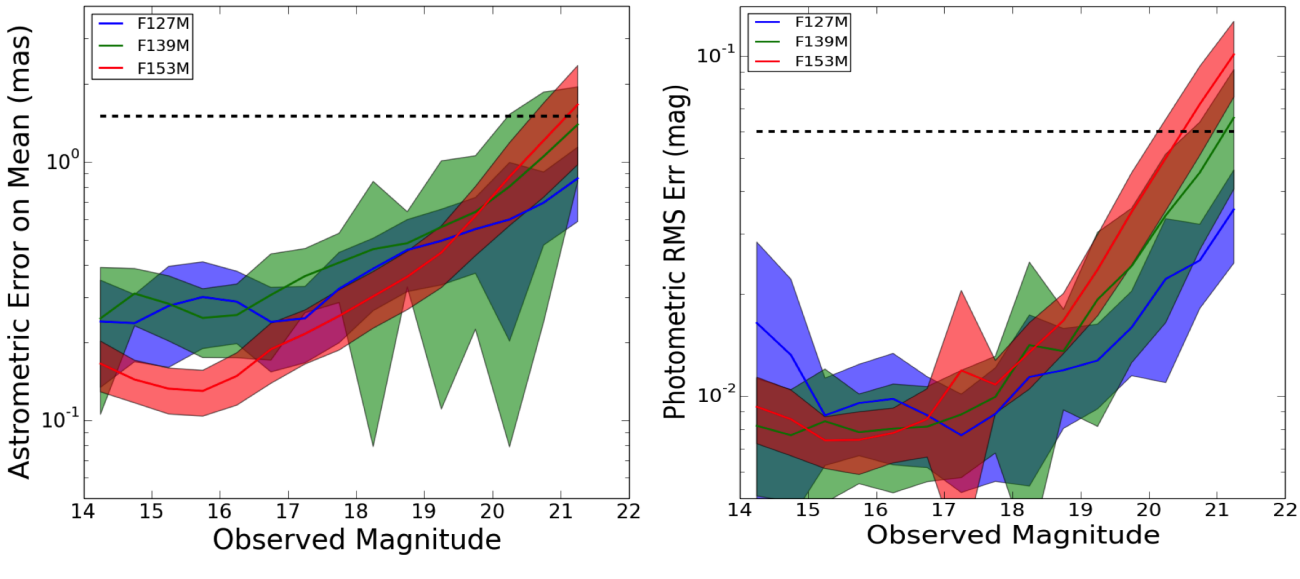

Fig. 16.— Astrometric Error on Mean and Photometric RMS error vs. observed magnitude for the F127M (blue), F139M (green), and F153M (red) filters. The solid lines represent the median error values in 0.5 magnitude bins, with the shaded region covering one standard deviation. Stars with astrometric errors above 1.5 mas (and thus proper motion errors above 0.65 mas yr^{-1}) or photometric errors above 0.06 mag in the F153M filter are not included in the analysis. These cuts are shown by the black dotted lines.

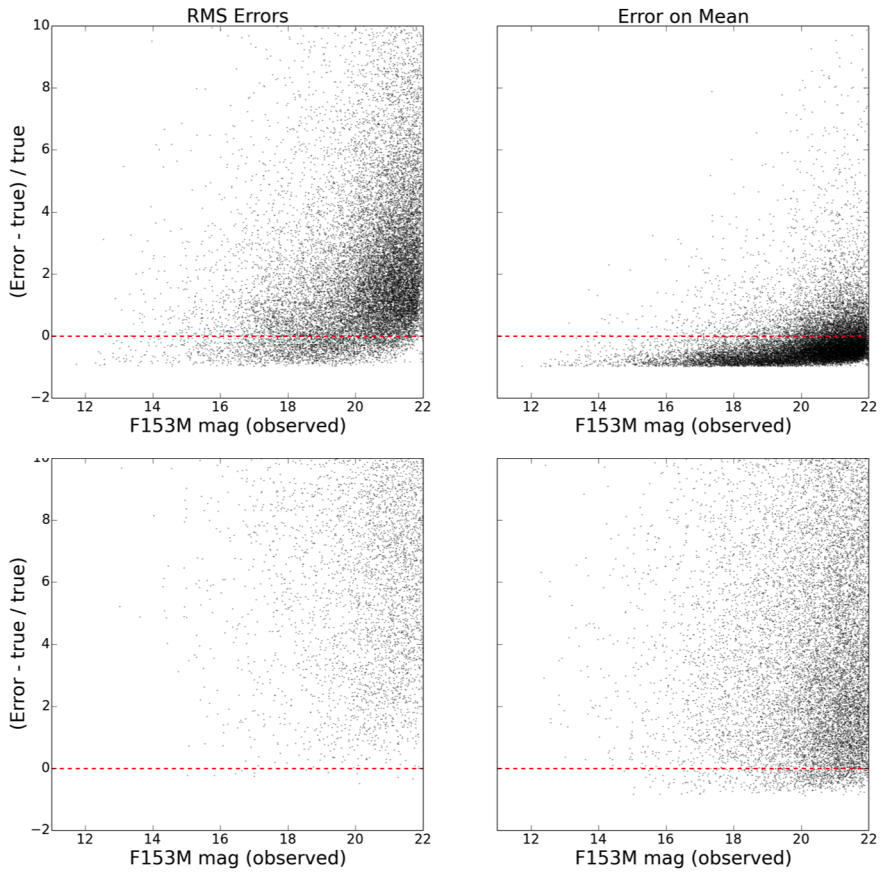

Fig. 17.— The fractional difference between the RMS error and error on the mean produced by *KS2* and the "true" errors for the photometry (top) and astrometry (bottom). For the photometry the "true" error for each star is considered to be the standard deviation of the observed magnitude and RMS position residuals across the F153M epochs. The photometric error on the mean is found to underestimate the true error while the astrometric RMS error is found to strongly overestimate the true error, and so the photometric RMS error and astrometric error on the mean are adopted for the individual epoch measurements.

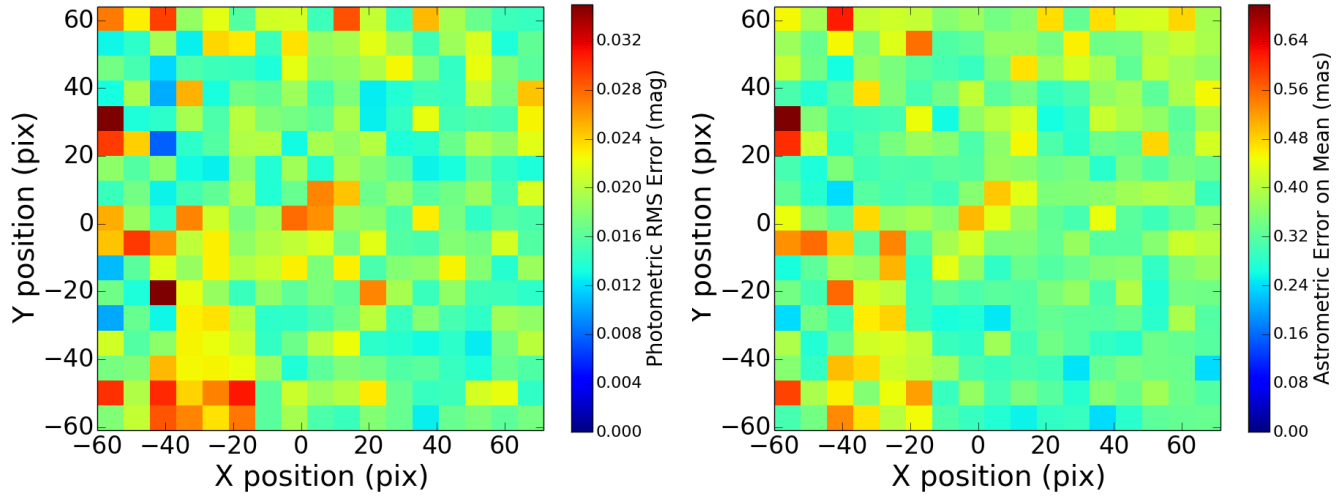

Fig. 18.— Average astrometric error (left) and F153M photometric error (right) as a function of position on the camera for all stars with F153M $<$ 20 mag. Average error values are calculated within 7" bins and are plotted relative to the cluster center. Higher errors are observed in the low reddening regions and the cluster center due to stellar crowding.

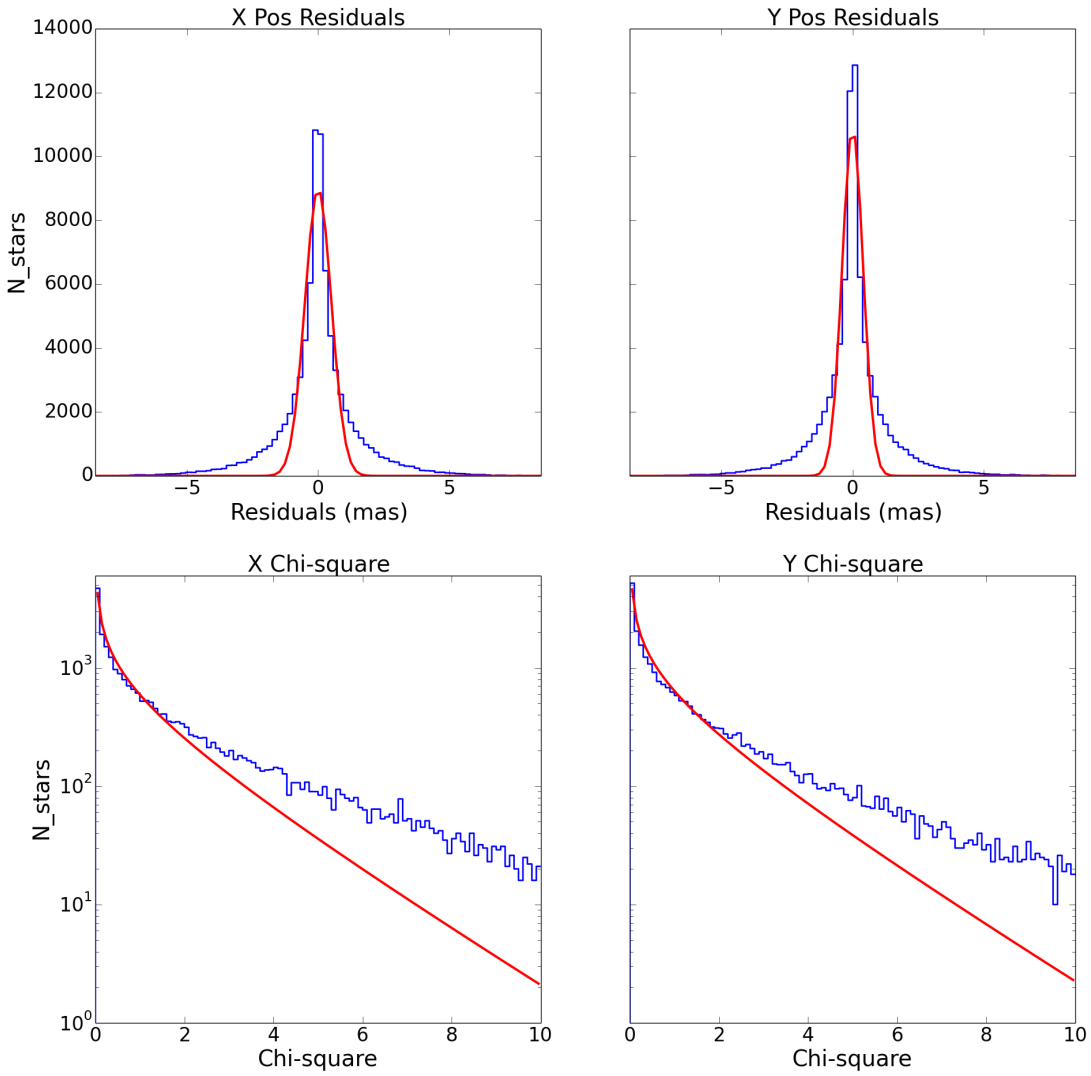

Fig. 19.— Positions residuals between the observed positions and those predicted from the calculated proper motions. *Top:* A histogram of the X and Y residuals. In an ideal situation these distributions would be gaussian (red line), but stellar crowding results in more power in the wings of the distribution. *Bottom:* The distribution of χ^2 values for the proper motion fits in both X and Y. As seen with the residuals, more high-value values are observed relative to the expected χ^2 distribution with 1 degree of freedom (red line), which can also be attributed to stellar crowding.

Appendix 2: Identification and Extinction of Red Clump Stars

The RC population is readily identified as a bar-like distribution in the F127M vs. [F127M - F153M] color-magnitude diagram (Figure 20). The bar is caused by differential reddening which smears out what would normally be a tight clump of stars along the reddening vector. However, it is not trivial to isolate the RC stars due to other objects intersecting the population (the Arches population intersects the RC stars from 2.0 < [F127M - F153M] < 2.5, for example). In order to identify RC stars, we calculate their F127M vs. [F127M - F153M] reddening vector by applying varying amounts of extinction to a model RC atmosphere, adopting the Nishiyama et al. (2009) extinction law. We use a PHOENIX model atmosphere (Allard et al. 2011) with T_{eff} = 4700 K and *log g* = 2.40 (cgs) to represent a typical solar-metallicity RC star. These values are based on the median properties of 42 RC stars with -0.05 ≤ [*Z*] ≤ 0.05 derived by Mishenina et al. (2006). Keeping the slope fixed, the y-intercept of the reddening vector is fit to the stars within a broad area around the RC population on the CMD (marked as red points in the right plot of Figure **??**). Arches cluster members identified by the proper motions analysis (see § 3.1) are eliminated from this sample. The reddening vector is found to fit the observed RC stars well. We conservatively identify RC stars as those within a rectangle with the long axis centered on the reddening vector with the short axis set by the least crowded section of the RC bar ([F127M - F153M] ≈ 2.7). This corresponds to a width of constant value ΔF127M = 0.7 mag.

The extinction of each RC star taken to be the extinction of the closest point on the reddening vector in the F127M - [F127M - F153M] CMD. Using this process we determine the extinction of 1027 RC stars identified across the field (Figure 21).

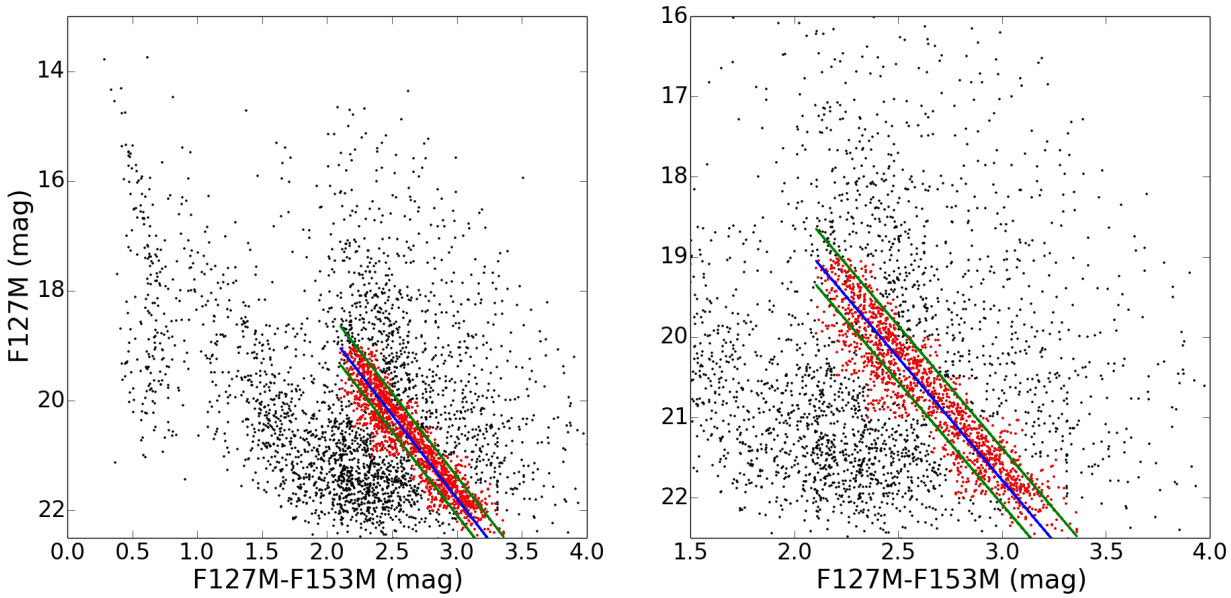

Fig. 20.— The identification of RC stars in the F127M vs. (F127M - F153M) CMD. Stars used in the initial fit of the RC star reddening vector are plotted as red points, while the RC reddening vector and final identification criterion are shown by the blue and green lines, respectively. Stars falling between the green lines are identified as RC stars.

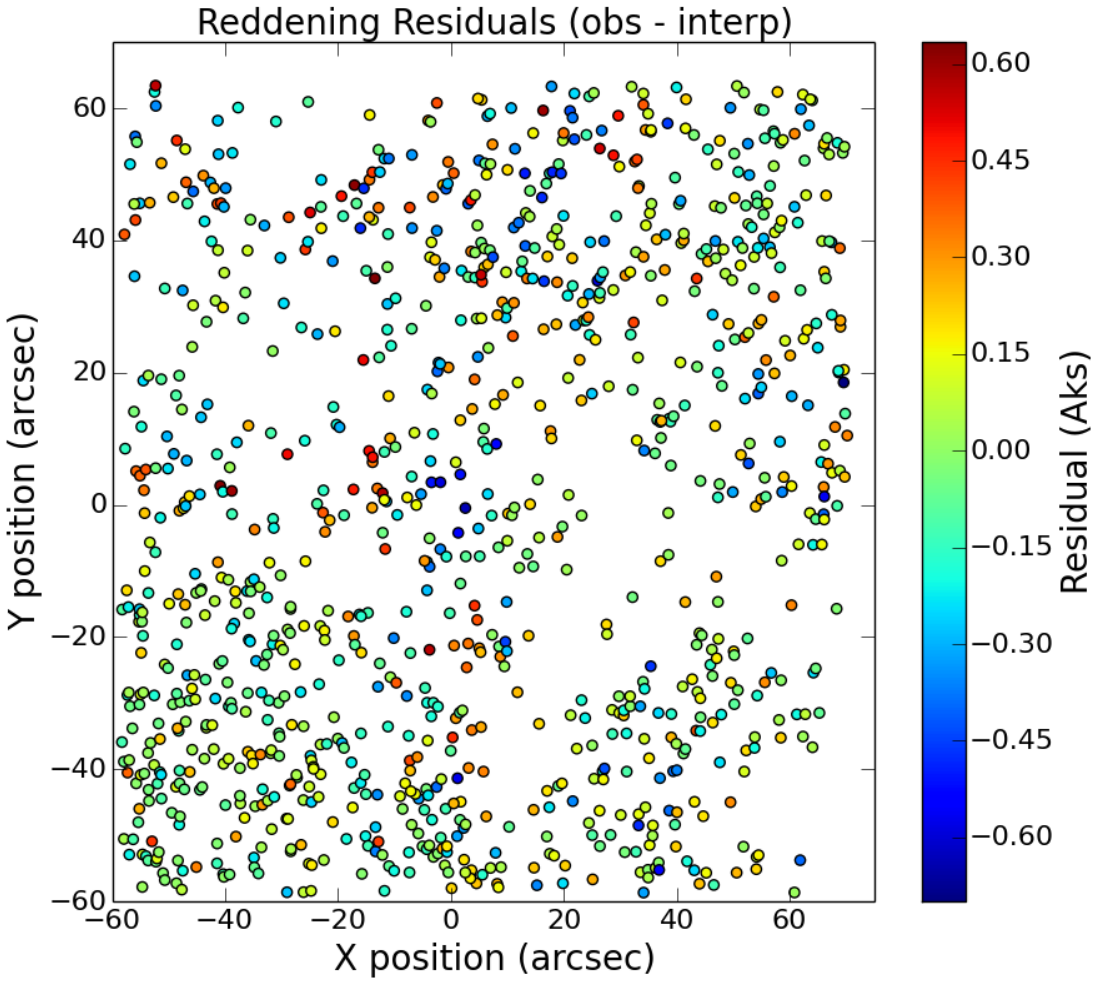

Fig. 21.— The positions of identified RC stars across the field. The color of each point corresponds to the derived A_{Ks}. Positions are plotted relative to the cluster center.

Appendix 3: Artificial Star and Observed Star Errors

The completeness analysis described in § 2.4 assumes that the measured artificial star errors match the observed star errors. A direct comparison of the errors reveals that the observed astrometric and photometric errors have an error floor that is not reproduced by the artificial star tests (Fig. 22). A possible explanation for this feature is residual PSF variations which are not captured by our spatially-varying PSF model ([APPENDIX 1]), as the artificial stars are planted using this model and thus wouldn't reflect this error. A constant error correction term of 0.14 mas and 0.008 mag is added to the artificial star position and magnitude uncertainties, after which the artificial star errors are found to closely follow those of the observed stars. This error correction does not have a noticeable effect on the completeness analysis as only stars far below the error cuts are significantly affected.

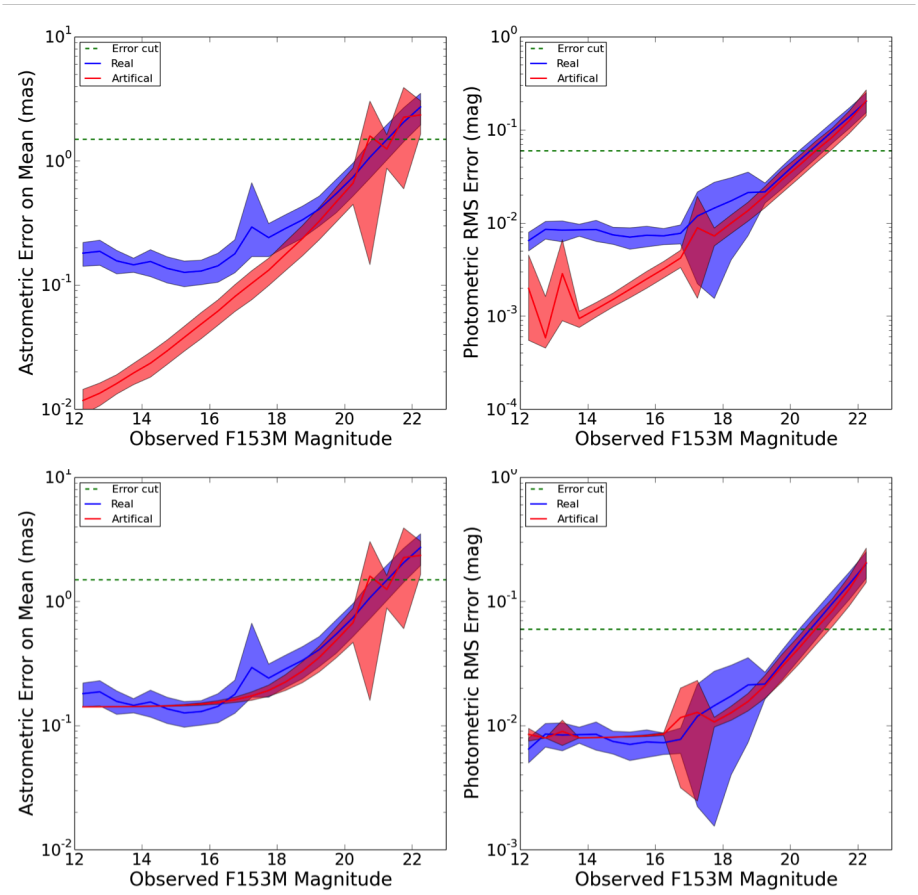

Fig. 22.— Astrometric and photometric errors for the observed and artificial stars, before (top) and after (bottom) the addition of a constant error term in the artificial star errors. The solid line and filled area represents the median and standard deviation of the error at each magnitude, respectively. The added error terms correspond to the error floor seen in the observed star measurements of 0.14 mas and 0.008 mag. After this adjustment the error distributions match well. The green dotted line shows the error cuts used in this study.

Appendix 4: Posteriors of Profile Fits

In this appendix we present the posterior distributions for the different profiles and models described in § 3.2 and § 3.3. The posteriors for the power law model (Equation 4) fit to the entire cluster sample is shown in Figure 23, while the power law fits to the high-mass and low-mass cluster members (to explore mass segregation) and the members parallel and perpendicular to the cluster's orbit (to explore tidal tails) are shown in Figure 24 and Figure 25, respectively. The posteriors for the EFF87 model (Equation 6) and King model (Equation 9) fit to the cluster sample are shown in Figures 26 and 27. The best-fit parameter values and errors are obtained from the mean and standard deviation of a gaussian fit to the posteriors and are summarized in [TABLE WITH ALL RESULTS].

In all plots, the output of the *Multinest* sampling is in black, the corresponding gaussian fit in red, and the input prior in green (if applicable). Amplitudes are calculated such that the total number of stars in the profile is equal to the total number of cluster members identified after correcting for membership probability, completeness, and area corrections (see Equation 4).

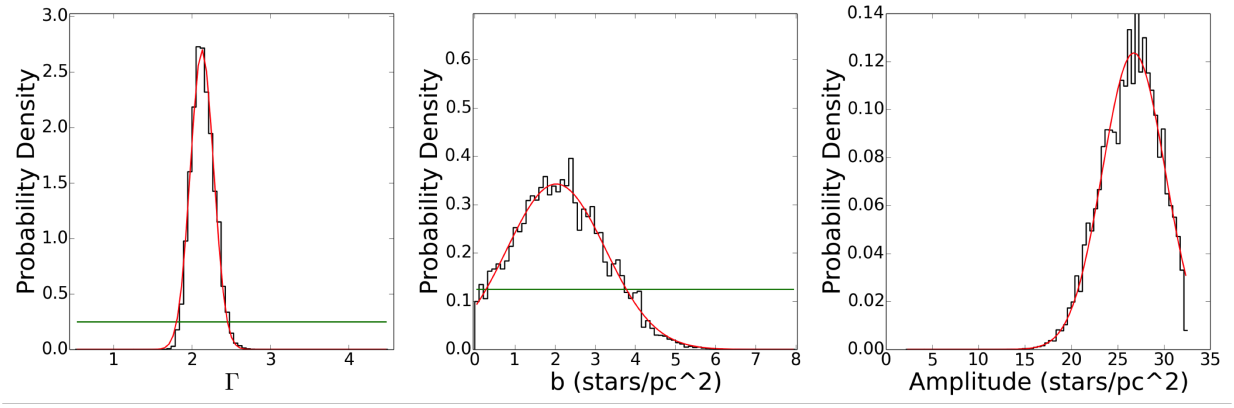

Fig. 23.— The posterior distributions for the power law model fit to the entire cluster sample.

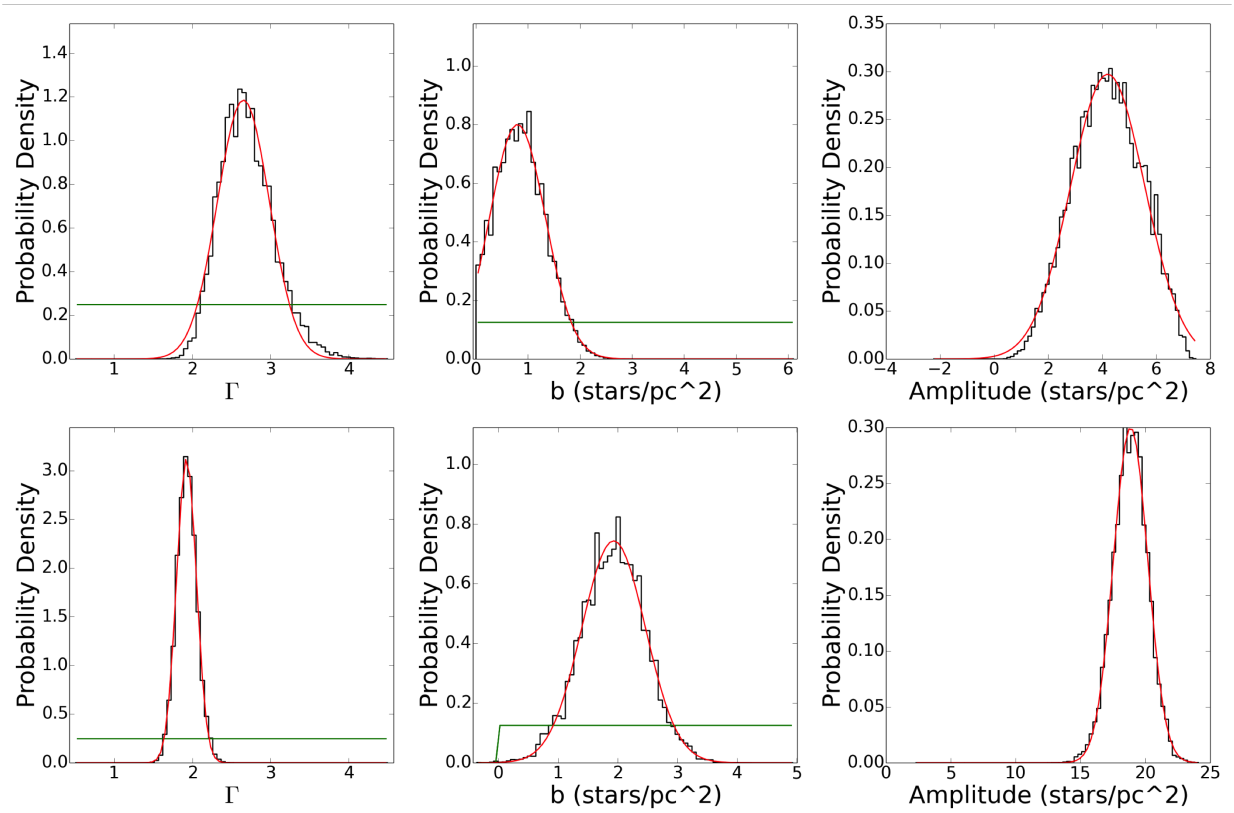

Fig. 24.— The posterior distributions for the power law model fits to the low-mass (top, F153M $>$ 17 mag) and high-mass (bottom, F153M $<$ 17 mag) cluster members. That the high-mass stars have a steeper power law slope Γ is an indication of mass segregation in the Arches cluster.

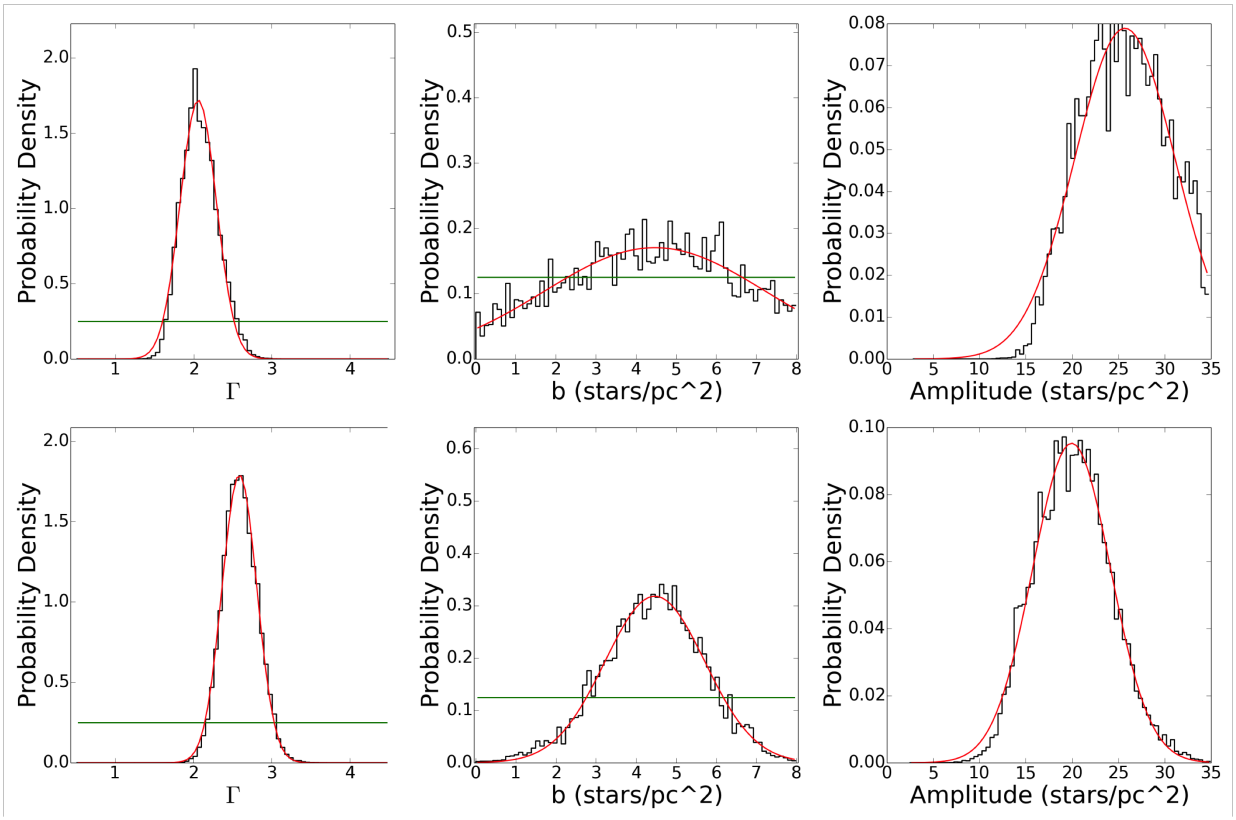

Fig. 25.— The posterior distributions for the power law model fits to the cluster members parallel (top) and perpendicular (bottom) to the bulk cluster orbit. The existence of tidal tails in the Arches would cause differences in the power law slopes Γ of these profiles. No significant difference is found, though it is quite possible that this sample is not deep enough or over a wide enough field of view to detect the tidal tails.

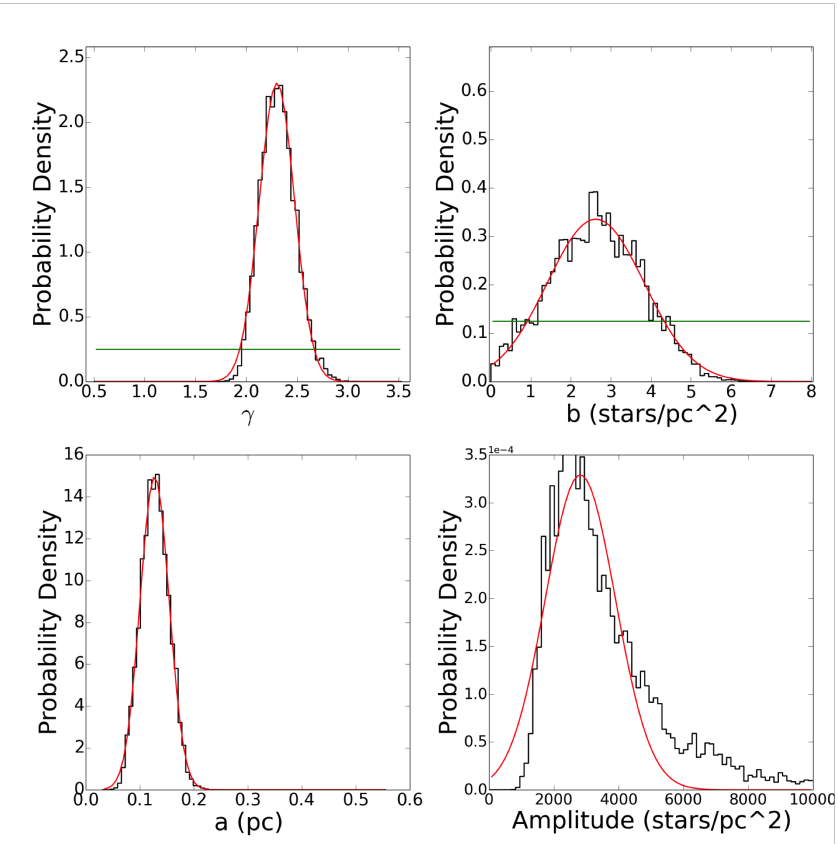

Fig. 26.— The posterior distributions for the EFF87 model fit.

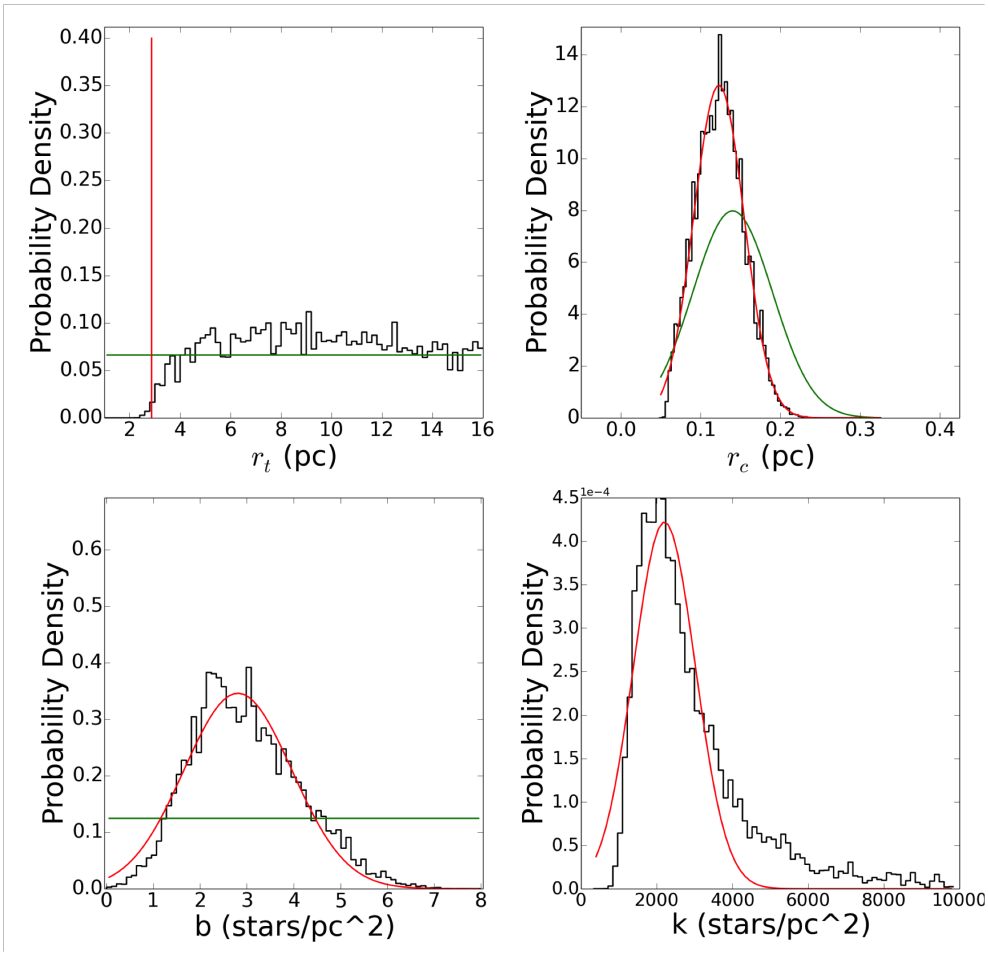

Fig. 27.— The posterior distributions for the King model fit. The 3σ limit to the tidal radius r_t (2.9 pc) is indicated by the red line, where 99.7% of the best-fit models fall above this value.